

Document downloaded from:

<http://hdl.handle.net/10251/48118>

This paper must be cited as:

Vilaplana Cerda, Rl.; Santamaría-Pérez, D.; Gomis Hilario, O.; Manjón Herrera, FJ.; González, J.; Segura, A.; Muñoz, A.... (2011). Structural and vibrational study of Bi₂Se₃ under high pressure. *Physical Review B*. 84:184110-1-184110-15.
doi:10.1103/PhysRevB.84.184110.



The final publication is available at

<http://journals.aps.org/prb/pdf/10.1103/PhysRevB.84.184110>

Copyright American Physical Society

Structural and vibrational study of Bi₂Se₃ under high pressure

R. Vilaplana,^{1,*} D. Santamaría-Pérez,² O. Gomis,¹ F.J. Manjón,³ J. González,^{4,5}
A. Segura,⁶ A. Muñoz,⁷ P. Rodríguez-Hernández,⁷ E. Pérez-González,⁷ V.
Marín-Borrás,⁸ V. Muñoz-Sanjose,⁸ C. Drasar,⁹ and V. Kucek⁹

¹ Centro de Tecnologías Físicas, MALTA Consolider Team, Universitat Politècnica de València, 46022 Valencia (Spain)

² Departamento de Química Física I, Universidad Complutense de Madrid, MALTA Consolider Team, Avenida Complutense s/n, 28040 Madrid, Spain

³ Instituto de Diseño para la Fabricación y Producción Automatizada, MALTA Consolider Team, Universitat Politècnica de València, 46022 Valencia (Spain)

⁴ DCITIMAC - MALTA Consolider Team, Universidad de Cantabria, Santander (Spain)

⁵ Centro de Estudios de Semiconductores, Universidad de los Andes, Mérida 5201 (Venezuela)

⁶ Instituto de Ciencia de Materiales de la Universidad de Valencia - MALTA Consolider Team - Departamento de Física Aplicada, Universitat de València, 46100 Burjassot, Valencia (Spain)

⁷ MALTA Consolider Team - Departamento de Física Fundamental II, Instituto Univ. de Materiales y Nanotecnología, Universidad de La Laguna, La Laguna, Tenerife (Spain)

⁸ Departamento de Física Aplicada, Universitat de València, 46100 Burjassot, Valencia (Spain)

⁹ Faculty of Chemical Technology, Department of Physics, University of Pardubice, Studentská 95, 53210-Pardubice, (Czech Republic)

Abstract. The structural and vibrational properties of bismuth selenide (Bi₂Se₃) have been studied by means of x-ray diffraction and Raman scattering measurements up to 20 and 30 GPa, respectively. The measurements have been complemented with *ab initio* total-energy and lattice dynamics calculations. Our experimental results evidence a phase transition from the low-pressure rhombohedral (R-3m) phase (α -Bi₂Se₃) with sixfold coordination for Bi to a monoclinic C2/m structure (β -Bi₂Se₃) with sevenfold coordination for Bi above 10 GPa. The equation of state and the pressure dependence of the lattice parameters and volume of α and β phases of Bi₂Se₃ are reported. Furthermore, the presence of a pressure-induced electronic topological phase transition in α -Bi₂Se₃ is discussed. Raman measurements evidence that Bi₂Se₃ undergoes two additional phase transitions around 20 and 28 GPa, likely towards a monoclinic C2/c and a disordered bcc structure with eightfold and nine-ten coordination,

* Corresponding author. E-mail address: rovilap@fis.upv.es
Tel.: + 34 96 652 84 26, Fax: + 34 96 652 84 09

respectively. These two high-pressure structures are the same that have been recently found at high pressures in Bi_2Te_3 and Sb_2Te_3 . On pressure release Bi_2Se_3 reverts back to the original rhombohedral phase after considerable hysteresis. Symmetries, frequencies, and pressure coefficients of the Raman and IR modes in the different phases are reported and discussed.

Key words: high pressure, topological insulators, thermoelectric materials, powder x-ray diffraction, Raman scattering, *ab initio* calculations

PACS: 63.20.-e, 62.50.-p, 78.30.-j

I. Introduction

Bismuth selenide (Bi_2Se_3) is one of the binary end members of the $(\text{Bi,Sb})_2(\text{Te,Se})_3$ family of semiconductors. These layered chalcogenides have a tremendous impact for thermoelectric applications, which are critical components for solid-state power generating and refrigerating devices [1]. Therefore, these semiconductors and their alloys have been extensively studied. However, due to the superiority of Bi_2Te_3 -based materials for these applications at room temperature [2,3] and of Sb_2Te_3 -based materials in the region between 400 and 500K [3,4], Bi_2Se_3 , while well studied, has not been subjected to the same degree of intensive research than the other two end members of the family.

Bi_2Se_3 is a narrow bandgap semiconductor with tetradymite crystal structure [R-3m, space group (S.G.) 166, Z=3] [5]. This rhombohedral layered structure is formed by *quintuple* layers; i.e., formed by 5 hexagonal close packed atomic sublayers (Se-Bi-Se-Bi-Se), linked by van der Waals forces. The same structure is common to other narrow bandgap semiconductor chalcogenides, like Bi_2Te_3 and Sb_2Te_3 , and has been found as a high pressure phase of As_2Te_3 [6]. Recently, it has been shown that these materials can be exfoliated like graphene and that a single layer exhibits high electrical conductivity and low thermal conductivity so that a new nanostructure route can be envisaged to improve dramatically the thermoelectrical properties of this compound by means of either charge carrier confinement or acoustic phonon confinement [7-12].

Bi_2Se_3 , as well as Bi_2Te_3 and Sb_2Te_3 , has been recently predicted to behave as topological insulators [13]; i.e. a new class of materials with unique properties resulting from the relativistic-like character and topological protection of their surface states. These topological insulators are characterized by the presence of a strong spin-orbit

coupling that leads to the opening of a narrow bandgap and causes certain topological invariants in the bulk to differ from their values in vacuum. The sudden change of invariants at the interface results in metallic, time reversal invariant surface states whose properties are useful for applications in spintronics and quantum computation [14,15]. Therefore, in the recent years a number of papers have been devoted to the search of the 3D topological insulators among Sb_2Te_3 , Bi_2Te_3 , and Bi_2Se_3 , and different works observed the features of the topological nature of the band structure in the three compounds [16-18]. Furthermore, it has been recently found that the bulk and surface conductance in these layered semiconductors can be explored by controlling the Fermi level after proper doping and that could lead to the discovery of new exotic states [19,20].

High-pressure studies are very useful to understand materials properties and design new materials because the increase in pressure allows to reduce the interatomic distances and to finely tune the materials properties. It has been verified that the thermoelectric properties of semiconductor chalcogenides improve with increasing pressure and that the study of the properties of these materials could help in the design of better thermoelectric materials by substituting external pressure by chemical pressure [21-25]. However, there are relatively few studies of layered chalcogenides Sb_2Te_3 , Bi_2Te_3 , and Bi_2Se_3 under pressure. The electrical and thermoelectric properties of Sb_2Te_3 , Bi_2Te_3 , and Bi_2Se_3 , as well as their electronic band structure, have been studied at high pressures [26-34] and recent high-pressure studies in these compounds have shown a pressure-induced superconductivity [35,36] that has further stimulated high-pressure studies [37]. However, the pressure dependence of many parameters of these layered chalcogenides is still not known.

Structural studies under pressure in layered chalcogenides Sb_2Te_3 , Bi_2Te_3 , and Bi_2Se_3 are scarce. In fact, the determination of the crystalline structures of these materials at high pressures has been a longstanding puzzle [22,30,38,39]. Only recently the space groups of the high-pressure phases of Bi_2Te_3 have been elucidated by powder x-ray diffraction (XRD) measurements at synchrotron radiation sources [40,41] specially with the use of particle swarm optimization algorithms for crystal structure prediction [41]. Furthermore, recent high-pressure powder XRD measurements have evidenced a pressure-induced electronic topological transition (ETT) in Bi_2Te_3 around 3.2 GPa as a change in compressibility [36,38,39,42,43]. An ETT or Lifshitz transition occurs when an extreme of the electronic band structure, which is associated to a Van

Howe singularity in the density of states, crosses the Fermi energy level [44]. This crossing, which can be driven by pressure, temperature, doping, etc., results in a change in the topology of the Fermi surface that changes the electronic density of states near the Fermi energy. An ETT is a 2.5 transition in the Ehrenfest description of the phase transitions so no discontinuity of the volume (first derivative of the Gibbs free energy) but a change in the compressibility (second derivative of the Gibbs free energy) is expected in the vicinity of the ETT. Anomalies in the phonon spectrum are also expected for materials undergoing an ETT [45,46] and have been observed in a number of materials [47,48,49] as well as in $\text{Sb}_{1.5}\text{Bi}_{0.5}\text{Te}_3$ [38]. In fact, recent Raman scattering measurements have confirmed that both Bi_2Te_3 and Sb_2Te_3 exhibit a pressure-induced ETT and that the high-pressure phases of Bi_2Te_3 up to 25 GPa are observed not only in Bi_2Te_3 but also in Sb_2Te_3 [50,51]. Up to our knowledge, there is no experimental high-pressure XRD study on Bi_2Se_3 under pressure reported in the literature and it remains to be confirmed whether Bi_2Se_3 (i) suffers an ETT like Bi_2Te_3 and Sb_2Te_3 , and (ii) undergoes the same structural transformations under pressure than Bi_2Te_3 and Sb_2Te_3 .

Vibrational studies under pressure in layered chalcogenides Sb_2Te_3 , Bi_2Te_3 , and Bi_2Se_3 are also scarce and have been recently reported for Sb_2Te_3 and Bi_2Te_3 [50-52]. Experimental and theoretical studies of the vibrational properties of Bi_2Se_3 have been reported at room pressure [53-59], but up to our knowledge there is neither an experimental nor a theoretical study of the lattice dynamics properties of Bi_2Se_3 under high pressure. As a part of our systematic study of the structural stability and the vibrational properties of the semiconductor chalcogenide family, we report in this work room-temperature powder XRD and Raman scattering measurements in Bi_2Se_3 up to 20 and 30 GPa, respectively, together with total-energy and lattice dynamical *ab initio* calculations at different pressures. We provide evidence of a pressure-induced electronic topological transition (ETT) in the rhombohedral phase of Bi_2Se_3 and confirm that the Bi_2Se_3 seem to follow the same sequence of pressure induced phase transitions as observed in its parent compounds Sb_2Te_3 and Bi_2Te_3 .

II. Experimental details

We have used single crystals of n-type Bi_2Se_3 that were grown using the Bridgman technique. A polycrystalline ingot was synthesized by the reaction of stoichiometric quantities of the constituting elements (5N). Afterwards, the polycrystalline material was annealed and submitted to the growth process in a vertical

Bridgman furnace. Preliminary room temperature measurements on single crystalline samples (15mm x 4mm x 0.3mm) yielded in-plane electrical resistivity $\rho_{\perp c} = 5.6 \cdot 10^{-6}$ Ωm and Hall coefficient $R_H(\mathbf{B} \parallel \mathbf{c}) = 0.23 \text{ cm}^3\text{C}^{-1}$. Providing that $n = 1/R_H e$, the latter results gives an electron concentration $n = 2.7 \cdot 10^{19} \text{ cm}^{-3}$.

Angle-dispersive powder XRD measurements on Bi_2Se_3 have been carried out with an Xcalibur diffractometer (Oxford Diffraction Limited). XRD patterns were obtained on a 135 mm Atlas CCD detector placed at 110 mm from the sample using $K_{\alpha 1}$: $K_{\alpha 2}$ molybdenum radiation. The x-ray beam was collimated to a diameter of 300 μm . High-pressure measurements on Bi_2Se_3 powder were performed in a modified Merrill-Bassett diamond anvil cell (DAC) up to 20 GPa. The diamond anvils used have 500 μm of culet size. The grey Bi_2Se_3 powder was placed in the 200 μm -diameter hole of the stain-steel gasket preindented to a thickness of 40 μm . Exposure times were typically of 1 hour. The DAC used for these experiments allows access to an angular range $4\theta = 50^\circ$. However, only the powder patterns below $2\theta = 18.3^\circ$ were considered, because of the appearance of the stain-steel peaks of the gasket. Background has been manually subtracted. The observed intensities were integrated as a function of 2θ in order to give conventional, one-dimensional diffraction profiles. The CrysAlis software, version 171.33.55 (Oxford Diffraction Limited), was used for the data collections and the preliminary reduction of the data. The indexing and refinement of the powder patterns were performed using the POWDERCELL [60], and FULLPROF [61] program packages.

For unpolarized room-temperature Raman scattering measurements at high pressures, we inserted a small flake of the single crystal (100 μm x 100 μm x 5 μm) in a membrane-type diamond anvil cell (DAC). The Raman measurements were performed in backscattering geometry with a power below 2 mW in order not to burn the sample. In our measurements we have used two setups: i) a Horiba Jobin Yvon LabRAM HR microspectrometer equipped with a TE-cooled multi-channel CCD detector and with a spectral resolution below 2 cm^{-1} . In this case, a HeNe laser (6328 \AA line) was used for excitation; ii) a Horiba Jobin Yvon T64000 triple axis spectrometer with resolution of 1 cm^{-1} . In this case, an Ar-Kr gas laser (6470 \AA line) was used for excitation.

In both XRD and Raman experiments we used a 4:1 methanol-ethanol mixture as pressure-transmitting medium, which ensures hydrostatic conditions up to 10 GPa and quasi-hydrostatic conditions between 10 and 25 GPa [62,63]. Pressure was determined by the ruby luminescence method [64].

III. *Ab initio* calculations

Recently, the structures of the high-pressure phases of Bi_2Te_3 up to 52 GPa have been reported [40,41] and confirmed to occur not only in Bi_2Te_3 but also in Sb_2Te_3 at high pressures [50,51]. The rhombohedral structure ($\alpha\text{-Bi}_2\text{Te}_3$) was suggested to transform to the $C2/m$ ($\beta\text{-Bi}_2\text{Te}_3$, S.G. 12, $Z=4$) and the $C2/c$ ($\gamma\text{-Bi}_2\text{Te}_3$, S.G. 15, $Z=4$) structures above 8.2 and 13.4 GPa, respectively [41]. Furthermore, a fourth phase ($\delta\text{-Bi}_2\text{Te}_3$) was found above 14.5 GPa and assigned to a disordered bcc structure ($\text{Im-}3\text{m}$, S.G. 229, $Z=1$) [40,41]. In order to explore the relative stability of these phases in Bi_2Se_3 we have performed *ab initio* total-energy calculations within the density functional theory (DFT) [65] using the plane-wave method and the pseudopotential theory with the Vienna *ab initio* simulation package (VASP) [66]. We have used the projector-augmented wave scheme (PAW) [67] implemented in this package. Basis set including plane waves up to an energy cutoff of 320 eV were used in order to achieve highly converged results and accurate description of the electronic properties. We have used the generalized gradient approximation (GGA) for the description of the exchange-correlation energy with the PBEsol [68] prescription. Dense special k-points sampling for the Brillouin zone (BZ) integration were performed in order to obtain very well converged energies and forces. At each selected volume, the structures were fully relaxed to their equilibrium configuration through the calculation of the forces and the stress tensor. In the relaxed equilibrium configuration, the forces on the atoms are less than $0.002 \text{ eV}/\text{\AA}$ and the deviation of the stress tensor from a diagonal hydrostatic form is less than 1 kbar (0.1 GPa). The application of DFT-based total-energy calculations to the study of semiconductors properties under high pressure has been reviewed in Ref. 69, showing that the phase stability, electronic and dynamical properties of compounds under pressure are well describe by DFT.

Since the calculation of the disordered bcc phase is not possible to do with the VASP code we have attempted to perform calculations for the bcc-like monoclinic $C2/m$ structure proposed in Ref. 41. Furthermore, since the thermodynamic phase transition between two structures occurs when the Gibbs free energy, G , is the same for both phases, we have obtained G for the different phases using a quasi-harmonic Debye model [70]. This model allows to obtain G at room temperature from calculations performed for $T=0 \text{ K}$ in order to discuss about the relative stability of the different phases proposed in the present work.

To test our calculations, we show in **Table I** the calculated lattice parameters in the different phases of Bi_2Se_3 at different pressures. For the sake of comparison we show in **Table I** other theoretical calculations and experimental results available. As far as the R-3m phase is concerned, our calculated lattice parameters are in relatively good agreement with experimental values from **Ref. 5** and are similar to those calculated in **Ref. 59** with GGA-PBE both with and without considering the spin-orbit (SO) coupling. Additionally, we give the calculated lattice parameters of Bi_2Se_3 in the C2/m and C2/c structures at 13.5 and 25.5 GPa, respectively, for comparison with experimental data. Note that in **Table I** the a and b parameters of the C2/m and C2/c structures at 13.5 and 25.5 GPa for Bi_2Se_3 are very similar to those reported by Zhu *et al.* for Bi_2Te_3 [41]; however, the c lattice parameter and β angle for monoclinic C2/m and C2/c structures differ from those obtained by Zhu *et al.*. The reason is that the results of our *ab initio* calculations are given in the standard setting for the monoclinic structures, in contrast with **Ref. 41**, for a better comparison to future experiments since many experimentalist use the standard setting.

We have also performed lattice dynamics calculations of the phonon modes in the R-3m, C2/m, and C2/c phases at the zone center (Γ point) of the BZ in order to confirm whether the experimentally measured Raman scattering of the high-pressure phases of Bi_2Se_3 can be explained with the proposed structures. Our theoretical results enable us to assign the Raman modes observed for the different phases of Bi_2Se_3 . Furthermore, the calculations provide information about the symmetry of the modes and polarization vectors which is not readily accessible in the present experiment. Highly converged results on forces are required for the calculation of the dynamical matrix. We use the direct force constant approach (or supercell method) [71]. The construction of the dynamical matrix at the Γ point of the BZ is particularly simple and involves separate calculations of the forces in which a fixed displacement from the equilibrium configuration of the atoms within the *primitive* unit cell is considered. Symmetry aids by reducing the number of such independent displacements, reducing the computational effort in the study of the analyzed structures considered in this work. Diagonalization of the dynamical matrix provides both the frequencies of the normal modes and their polarization vectors. It allows to us to identify the irreducible representation and the character of the phonons modes at the Γ point. In this work we provide and discuss the calculated frequencies and pressure coefficients of the Raman-active modes for the three calculated phases of Bi_2Se_3 . The theoretical results obtained for infrared-active modes

for the three calculated phases of Bi_2Se_3 are given as supplementary material of this article [72].

As already commented in our previous papers [50,51], we have also checked the effect of the SO coupling in the structural stability and the phonon frequencies of the R-3m phase of Bi_2Se_3 . We have found that the effect of the SO coupling is very small and do not affect significantly our results (small differences of 1-3 cm^{-1} in the phonon frequencies at the Γ point). However, calculations especially for the phases with a lot of atoms in the unit cell are more time consuming. Therefore, the theoretical values corresponding to lattice dynamics calculations in the present paper do not include the SO coupling except those corresponding to the R-3m phase. Note that calculations without SO coupling are more justified than in the case of Sb_2Te_3 and Bi_2Te_3 [50,51] by the fact that the SO coupling is smaller in Bi_2Se_3 than in Sb_2Te_3 and Bi_2Te_3 .

IV. Results and discussion

A. X-ray diffraction in Bi_2Se_3

Figure 1 shows the x-ray powder diffraction data of Bi_2Se_3 up to 20 GPa. The room pressure x-ray pattern of $\alpha\text{-Bi}_2\text{Se}_3$ has been indexed with a rhombohedral structure (S.G. $R\text{-}3m$ (166)), and with lattice parameters $a = 4.123(1) \text{ \AA}$, $c = 28.486(1) \text{ \AA}$, and $V_0 = 419.3(2) \text{ \AA}^3$. These values are slightly smaller than those from Nakajima et al. ($a = 4.143 \text{ \AA}$, $c = 28.636 \text{ \AA}$, and $V_0 = 425.673 \text{ \AA}^3$) [5]. The initial rhombohedral structure is stable up to 9.7 GPa, where a phase transition occurs. The onset on the phase transition is placed at 9.7 GPa, the two phases (the initial and the high-pressure ones) coexisting up to at least 12 GPa. As can be seen in **Fig. 1**, the phase transition is fully reversible after increasing pressure to 20 GPa and releasing pressure to room pressure. We have indexed the diffraction patterns between 10 and 20 GPa as corresponding to the monoclinic $C2/m$ phase. **Figure 2** shows a full Rietveld refinement with the $C2/m$ structure of the XRD pattern obtained at 13.5 GPa and carried out using the program FULLPROF along with the obtained residuals. Lattice parameters and atomic positions obtained from the Rietveld refinement are shown in **Table II**.

Figures 3 and 4 show the experimental and theoretical pressure dependence of the volume and lattice parameters in both $\alpha\text{-Bi}_2\text{Se}_3$ and $\beta\text{-Bi}_2\text{Se}_3$, respectively, while the inset of **Fig. 4(a)** shows the c/a ratio vs. pressure dependence. Our measured pressure dependence of the volume, lattice parameters, and c/a ratio agree nicely with those predicted by total-energy *ab initio* calculations (see solid lines in **Figs. 3 and 4**). Fit of

the volume vs. pressure in α -Bi₂Se₃ to a Birch-Murnaghan equation of state (BM-EOS) yields the following data for the volume, bulk modulus and its pressure derivative at room pressure: $V_0 = 420(1) \text{ \AA}^3$, $B_0 = 53(8) \text{ GPa}$, $B'_0 = 2.9(2)$. Similarly, fit of the volume vs. pressure in β -Bi₂Se₃ to a BM-EOS yields following data for the volume, bulk modulus and its pressure derivative at room pressure: $V_0 = 529(2) \text{ \AA}^3$, $B_0 = 66(3) \text{ GPa}$, $B'_0 = 4.5$ (fixed). These results are compared to our theoretical results and other results published in the literature in **Table I**. We have also studied the axial compressibilities for α -Bi₂Se₃ by fitting to a BM-EOS the volume of a pseudo-cubic cell vs. pressure where the volume of this pseudo-cubic cell is calculated for axis a and c as $V_a = a^3$ and $V_c = c^3$, respectively [73]. The obtained results for the bulk modulus and its pressure derivative at room pressure are for c axis $B_0 = 26(2) \text{ GPa}$ and $B'_0 = 9(1)$ and for a axis $B_0 = 62(2) \text{ GPa}$ and $B'_0 = 4$ (fixed). As can be observed, the c axis is more compressible than the a axis.

It is known that a pressure-induced electronic topological transition occurs in α -Bi₂Te₃ and α -Sb₂Te₃, whose structure is the same as in α -Bi₂Se₃ [36,38,39,42,43]. Recently, it has been observed that the ETT in α -Bi₂Te₃ leads to a change in compressibility around 3.2 GPa without a change in volume but with a pronounced change in the c/a ratio behavior at pressures below and above the ETT [39,43]. Notably, we observe similar changes in the compressibility and in the c/a ratio around 5 GPa (around 4 GPa in theoretical calculations) in Bi₂Se₃ that suggest the presence of an ETT in this compound near 5 GPa. In order to confirm whether α -Bi₂Se₃ undergoes an ETT we have performed a more accurate analysis of the volume and lattice parameters vs. pressure up to 8 GPa, plotted in **Figs. 3 and 4**. In this sense, we have performed a linearization of the BM-EOS vs. the Eulerian strain:

$$H = B_0 + \frac{3}{2} B_0 (B'_0 - 4) f_E \quad (1)$$

where

$$H = \frac{P}{3 \cdot f_E \cdot (1 + 2 \cdot f_E)^{5/2}} \quad (2)$$

is the reduced pressure, and

$$f_E = \frac{(X^2 - 1)}{2} \quad (3)$$

is the Eulerian strain, with

$$X = \left(\frac{V_0}{V} \right)^{1/3} \quad (4)$$

Plotted in this way, the reduced pressure H vs. the Eulerian strain, f_E , should be linear for any stable compound. Furthermore, taking into account **Eq. (1)** we can obtain the bulk modulus of the compound at zero pressure, B_0 , and its pressure derivative, B_0' . Top panel of **Fig. 5** shows the $H(f_E)$ plot for the volume. In that plot it is observed a rather clear change in the slope of H around 3.4 GPa thus suggesting the presence of an ETT near 3.4 GPa. The obtained values for B_0 and B_0' by using Eq. 1 from the volume data before and after 3.4 GPa are: $B_0 = 59(1)$ GPa, $B_0' = -0.2(1)$ and $B_0 = 53(1)$ GPa, $B_0' = 3.1(8)$, respectively. Middle and bottom panels of **Fig. 5** show the $H(f_E)$ plot for the a (H_a) and c (H_c) axes, respectively. To obtain the reduced pressure for the a and c axes, we have used **Eqs. (2) to (4)** but with $X_a = a_0/a$ and $X_c = c_0/c$ for the a and c axes, respectively. Analyzing the pressure dependence of H_a and H_c in **Fig. 5** it can be observed that the change of the slope of H is related to the change found in H_a while H_c shows no change in compressibility between 0 and 8 GPa. For the case of the a lattice parameter the values for B_0 and B_0' obtained by using **Eq. (1)** from the a axis data before and after the 2.2 GPa are: $B_0 = 109(9)$ GPa, $B_0' = -12(5)$ and $B_0 = 80(2)$ GPa, $B_0' = -0.6(1)$, respectively. It is seen that in some cases a negative value for the B_0' is obtained which has not physical meaning as we expect the B_0 parameter to increase as pressure increases. Note that the straight lines in **Fig. 5** are tentatively drawn and we would have needed more experimental points to describe the change in the slope with less uncertainty. Therefore, further experiments in a synchrotron source are needed in order to obtain more accurate values for the B_0 and B_0' parameters both before and after the pressure at which the ETT occurs. For the case of the c axis where no change in slope is found the values for B_0 and B_0' calculated from **Eq. (1)** are $B_0 = 27.1(8)$ GPa and $B_0' = 8.0(1.2)$. The latter values are in good agreement with those obtained from the BM-EOS fit. Therefore, the analysis of the reduced pressures for a and V as a function of the Eulerian strain gives us a qualitative picture that supports the presence of the ETT due to the change of the slope in both figures, thus confirming that the change of the c/a ratio with pressure is a good indicator of the ETT since it is caused by the anomalous behavior of a as a function of pressure, which in turn results in a change in the compressibility at the ETT.

In conclusion, our XRD measurements reveal the occurrence of an ETT in α -Bi₂Se₃ which is related to a change in the layer compressibility, as it occurs in α -Bi₂Te₃ [43]. The presence of an ETT in α -Bi₂Se₃ is in agreement with previously reported electrical resistivity measurements [28]. On the other hand, we have found a phase transition above 9.7 GPa in α -Bi₂Se₃ which seems to have the C2/m structure; i.e., the same structure found in α -Bi₂Te₃ above 9 GPa [41].

B. Raman scattering of α -Bi₂Se₃

The rhombohedral structure of Bi₂Se₃ is a centrosymmetric structure, and group theory allows 10 zone-center modes which decompose in the irreducible representations as follows [53,54]

$$\Gamma_{10} = 2A_{1g} + 3A_{2u} + 2E_g + 3E_u \quad (1)$$

The two acoustic branches come from one A_{2u} and a doubly degenerated E_u mode, while the rest correspond to optic modes. Gerade (g) modes are Raman active while ungerade (u) modes are infrared (IR) active. Therefore, there are four Raman-active modes (2A_{1g} + 2E_g) and four IR-active modes (2A_{2u} + 2E_u). The E_g modes correspond to atomic vibrations in the plane of the layers, while the A_{1g} modes correspond to vibrations along the c axis perpendicular to the layers [53,54].

Figure 6 shows the experimental Raman spectra of rhombohedral Bi₂Se₃ at different pressures up to 8.6 GPa. We have observed and followed under pressure 3 out of the 4 Raman-active modes. The E_g mode calculated to be close to 40 cm⁻¹ has not been observed in our experiments neither in previous Raman scattering measurements at room pressure in bulk material [6,54]; however, this mode has been observed recently in nanoplatelets [56]. **Figure 7(a)** shows the experimental pressure dependence of the frequencies of the 3 first-order Raman modes measured in α -Bi₂Se₃ and **Table III** summarizes our experimental and theoretical first-order Raman mode frequencies and pressure coefficients in the rhombohedral phase. Our experimental frequencies at room pressure are in good agreement with those already measured in **Ref. 54 and 56** (see **Table III**). On the other hand, our theoretical frequencies at room pressure are also in good agreement with those reported in **Ref. 59** both with and without SO coupling (see **Table III**).

In **Fig. 7(a)** it can be observed that all the measured Raman modes exhibit a hardening with increasing pressure. The experimental values of the frequencies and pressure coefficients are in a general good agreement with our theoretical calculations (see **Table III**); however, it can be noted a decrease of the pressure coefficient of the A_{1g}^1 and E_g^2 modes around 5 GPa [see dashed lines in **Fig. 7(a)**]. Anomalies in the phonon spectrum are also expected for materials undergoing an electronic topological transition [45,46] and have been observed in a number of materials [47,48] as well as in $Sb_{1.5}Bi_{0.5}Te_3$ [38]. Therefore, we have attributed the less positive pressure coefficient of these two Raman modes to a pressure-induced ETT. In fact, in previous studies in Sb_2Te_3 and Bi_2Te_3 under pressure we have experimentally measured a change in the pressure coefficient of the frequency of several modes [50,51]. In order to support our hypothesis we also plot in **Fig. 7(b)** the pressure dependence of the linewidth of the three measured Raman modes. Curiously, it is observed that the FWHM changes its slope around 5 GPa; thus confirming an anomaly related to the ETT as was also evidenced in Sb_2Te_3 and Bi_2Te_3 under pressure [50,51]. Therefore, both our results of the pressure dependence of the frequency and the linewidth give support to the observation of the ETT around 5 GPa in α - Bi_2Se_3 similarly to the case of α - Sb_2Te_3 [50] and α - Bi_2Te_3 [51].

The large linewidth of the first-order Raman modes at ambient pressure can only be accounted for by a rather strong phonon-phonon interaction (i.e. anharmonic decay) causing a decrease of the phonon lifetimes. This is likely due to the coincidence of the first-order Raman-mode frequencies with a high density of the two-phonon (sum) density of states. In this sense, the decrease of the linewidth of the Raman-active modes with increasing pressure can be understood by the separation of the first-order Raman-active modes with respect to the frequency of the high density of the two-phonon (sum) density of states due to the larger pressure coefficient of the first-order Raman modes than the sum of two-phonon states which usually involves acoustic modes with very small or even negative pressure coefficients [74].

Similarly to the case of α - Sb_2Te_3 [50] and α - Bi_2Te_3 [51], our results for α - Bi_2Se_3 show that the high-frequency A_{1g} mode is almost not altered near the ETT in good agreement with our calculations; however, we have noted a clear change of the pressure coefficient of the frequency for both the lower A_{1g} and the higher-frequency E_g modes. Since A_{1g} modes are polarized in the direction perpendicular to the layers while the E_g modes are polarized along the layers, our observation of a less positive pressure

coefficient of both types of modes in Bi_2Se_3 could suggest that the ETT in Bi_2Se_3 is related to a change of the structural compressibility of both the direction perpendicular to the layers and the direction along the layers. This seems not to be in agreement with our results of XRD neither with those of Polian *et al.* for Bi_2Te_3 [43] where the ETT only affects the compressibility of the plane of the layers. In this sense, it can be observed that the change of pressure coefficient around 5 GPa in Bi_2Se_3 is bigger for the E_g mode than for the A_{1g} modes in good agreement with the larger change in compressibility along the layers than in the direction perpendicular to the layers. However, the same is not true in the case of Bi_2Te_3 where the change of the pressure coefficient at 4 GPa in Bi_2Te_3 is bigger for the A_{1g} mode than for the E_g mode [51]. Consequently, more work is needed to understand the mechanism of the ETT in this material.

It is timely to conclude this section by comparing the Raman mode frequencies and their pressure coefficients in $\alpha\text{-Bi}_2\text{Se}_3$ with those of $\alpha\text{-Sb}_2\text{Te}_3$ [50] and $\alpha\text{-Bi}_2\text{Te}_3$ [51] and with other layered materials. It is known that in chalcogenide laminar materials, the two lowest-frequency E and A modes are usually related to shear vibrations between adjacent layers along the a-b plane and to vibrations of one layer against the others along the c axis, respectively. It has been commented that the E mode displays the smallest pressure coefficient which is consistent with the weak bending force constant between the interlayer distances (in our case, Se-Se distances) while the A mode displays the largest pressure coefficient due to the extraordinary increase of the stretching force constant between the interlayer distances [50,51]. For example, the E and A modes with frequencies around 40 (60) cm^{-1} and 116 (133) cm^{-1} in InSe (GaSe), respectively, have pressure coefficients of 0.68 (0.85) $\text{cm}^{-1}/\text{GPa}$ and 5.41 (5.78) $\text{cm}^{-1}/\text{GPa}$ [75,76]. In $\alpha\text{-Bi}_2\text{Se}_3$ our theoretical calculations show that the two lowest-frequency A_{1g} and E_g modes have rather similar pressure coefficients in comparison to other layered chalcogenides like InSe and GaSe. This result is consistent with smaller anisotropy in the intralayer and interlayer properties of Bi_2Se_3 than in InSe and GaSe. We arrived at a similar conclusion in our study of $\alpha\text{-Sb}_2\text{Te}_3$ [50] and $\alpha\text{-Bi}_2\text{Te}_3$ [51] and we have attributed it to the stronger interlayer interaction occurring in Bi_2Se_3 , Bi_2Te_3 and Sb_2Te_3 favored by the SO coupling which is absent in other laminar chalcogenides, like InSe and GaSe.

Finally, regarding the Raman modes of the rhombohedral structure in Bi_2Se_3 , Bi_2Te_3 , and Sb_2Te_3 , we have plotted in **Fig. 8** the frequencies of the Raman-active

modes in the three compounds as a function of the total mass of the (Bi,Sb)-(Se,Te) molecule and its reduced mass. It can be observed that the theoretical values obtained for the lowest-frequency E_g^1 mode scale with the total mass of the molecule ($m_T=m_C+m_A$; C=cation, A=anion) so both anion and cation have a considerable contribution to this mode, and especially the cation in Bi_2Se_3 and Bi_2Te_3 . Contrarily, the experimental and theoretical frequencies of the other three modes scale with the reduced mass μ of the molecule ($1/\mu=1/m_C+ 1/m_A$). This especially true for the A_{1g} modes and it means that in these modes the anion movement has a slightly larger contribution than the cation. As regards the pressure coefficients of the Raman-active modes, the E_g^1 mode has a value around $2 \text{ cm}^{-1}/\text{GPa}$ in the three compounds being larger for Sb_2Te_3 and smaller for Bi_2Se_3 . On the other hand, the A_{1g}^1 mode has values between 3.2 and $4.5 \text{ cm}^{-1}/\text{GPa}$ in the three compounds being again larger for Sb_2Te_3 and smaller for Bi_2Se_3 . Our results show that the difference of pressure coefficient between the interlayer mode (A_{1g}^1) and the intralayer mode (E_g^1) is larger for Sb_2Te_3 and smaller for Bi_2Se_3 and this result suggests that, despite being the compound with the smaller SO coupling, Bi_2Se_3 is the compound showing smaller anisotropy in the interlayer and intralayer properties. However, the smaller pressure coefficients of the lower-frequency modes in Bi_2Se_3 than in Bi_2Te_3 and Sb_2Te_3 , which are more influenced by interlayer vibrations, suggest that the interlayer bonds of van der Waals type tend to harden at a smallest rate with pressure in Bi_2Se_3 than in the other two compounds; i.e., the anisotropy in the properties along the layers and perpendicular to the layers tend to disappear more slowly with increasing pressure in Bi_2Se_3 than in Bi_2Te_3 and Sb_2Te_3 . On the other hand, it is curious to note that the experimental pressure coefficients of the E_g^2 and the A_{1g}^2 modes are rather similar in the three compounds. In particular, for the A_{1g}^2 mode it is the same ($2.9 \text{ cm}^{-1}/\text{GPa}$) for the three compounds although our calculations suggest that it should be somewhat smaller for Sb_2Te_3 . Since these two high-frequency modes are mainly related to intralayer vibrations, their similar pressure coefficients suggest a rather similar covalent nature of the intralayer bonds in the three compounds.

B. Raman scattering of β - Bi_2Se_3

It has been recently demonstrated in a joint experimental and theoretical work that α - Bi_2Te_3 undergoes a phase transition around 7.5 GPa towards a β - Bi_2Te_3 phase with monoclinic $C2/m$ structure [41]. **Figure 9(a)** shows the experimental Raman spectra of β - Bi_2Se_3 at different pressures from 10 to 19 GPa , which according to our x-

ray powder diffraction measurements correspond to Raman active modes of the C2/m structure. In the monoclinic C2/m structure, all Bi and Se atoms occupy 4i Wyckoff sites. Therefore, group theoretical considerations predict 30 vibrational modes with the following representation

$$\Gamma_{30} = (10A_g + 10B_u) + (5B_g + 5A_u). \quad (2)$$

From them, one A_u and two B_u are the acoustic phonons and the rest are optical phonons. Consequently, we expect 15 zone-center Raman-active ($10A_g + 5B_g$) modes for the C2/m phase. For the sake of comparison we have marked in **Fig. 9(a)** the calculated Raman mode frequencies for this phase at 9.8 GPa to compare it with the Raman spectrum at 9.8 GPa. It can be observed that the frequencies of the experimental Raman modes agree reasonably with our calculations. **Figure 9(b)** shows the pressure dependence of the experimental and theoretical Raman mode frequencies in β -Bi₂Se₃. It can be observed that there is a consistent agreement between the experimental and theoretical Raman mode frequencies and its pressure coefficients. Therefore, we can reasonably confirm that the β -Bi₂Se₃ phase has the monoclinic C2/m structure already found in Bi₂Te₃ by means of XRD measurements [41]. **Table IV** summarizes the experimental and theoretical first-order Raman mode frequencies and pressure coefficients at 9.8 GPa in β -Bi₂Se₃.

In our experiments we have not observed the four lowest-frequency modes (A_g^1 , B_g^1 , A_g^2 , B_g^2), whose detection is difficult because they could be weak and their frequencies are below the cutting edge of our Raman edge filter of the LabRAM spectrometer. However, other weak low-frequency modes (A_g^3 , A_g^4 , and B_g^3) can be clearly followed under pressure. Finally, all the highest-frequency modes are relatively intense and could be followed under pressure, with the only exception of the B_g^5 mode which is likely masked by the stronger A_g^6 and A_g^7 modes [see **Figs. 9(a) and (b)**]. The frequencies and pressure coefficients of these high-frequency modes are in very good agreement with our calculations [see **Fig. 9(b) and Table IV**], except the pressure coefficients of the B_g^4 and A_g^5 modes. These results support our assignment of β -Bi₂Se₃ to the C2/m phase. A decomposition of the Raman spectrum of the β -Bi₂Se₃ phase at 13.5 GPa into Voigt profiles can be observed in **Fig. 1** in the supplementary material [72].

Finally, we want to make a comment on the Bi coordination of β -Bi₂Se₃. In this respect, at the R-3m to C2/m phase transition pressure between 10 and 12 GPa, the highest-frequency mode of β -Bi₂Se₃ has a smaller frequency (198 cm⁻¹) than the highest-frequency mode of α -Bi₂Se₃ (203 cm⁻¹). This decrease in frequency of the highest-frequency mode, usually related to stretching Bi-Se vibrations, suggests an increase in the Bi-Se distance related to an increase of the Bi coordination from sixfold in α -Bi₂Se₃ to sevenfold in β -Bi₂Se₃. This result is in good agreement with the recently observed increase of the Bi coordination on going from α -Bi₂Te₃ to β -Bi₂Te₃ [41,51] and of the Sb coordination on going from α -Sb₂Te₃ to β -Sb₂Te₃ [50].

C. Raman scattering of γ -Bi₂Se₃ and δ -Bi₂Se₃

Similarly to the β phase, it has been recently demonstrated in a joint experimental and theoretical work that β -Bi₂Te₃ undergoes a phase transition around 13.4 GPa towards a γ -Bi₂Te₃ phase with monoclinic C2/c structure [41]. We have observed that the Raman spectrum above 19.9 GPa is different from that of the C2/m phase. **Figure 10(a)** shows the experimental Raman spectra of γ -Bi₂Se₃ at different pressures from 19.9 to 27.8 GPa. Furthermore, it can be observed that the Raman spectrum has almost disappeared at 27.8 GPa thus suggesting a phase transition to a Raman-inactive phase above this pressure. Additionally, on pressure release we have observed that the sample reverts back to the original rhombohedral phase below 5 GPa after considerable hysteresis. The spectrum of the recovered sample in the rhombohedral phase at 1 atm after releasing pressure is shown as the last spectrum in the top of **Fig. 10(a)**.

Group theoretical considerations predict 30 vibrational modes for the monoclinic C2/c phase with the following representation [50,51]

$$\Gamma_{30} = (7A_g + 7A_u) + (8B_g + 8B_u). \quad (3)$$

There are one A_u and two B_u acoustic modes and the rest are optical modes. Therefore, we expect 15 zone-center Raman-active modes (7A_g + 8B_g) for the C2/c phase.

For the sake of comparison we have marked in **Fig. 10(a)** the calculated Raman mode frequencies for the C2/c phase at 20 GPa to compare it with the Raman spectrum at 19.9 GPa. It can be observed that the frequencies of the experimental Raman modes

agree reasonably with our calculations at this pressure thus giving support to the assignment of the γ -Bi₂Se₃ to the C2/c phase. Further, it can be noted that, at 20 GPa, the highest-frequency mode of γ -Bi₂Se₃ has a smaller frequency (210 cm⁻¹) than the highest-frequency mode of β -Bi₂Se₃ (around 220 cm⁻¹). This decrease in frequency of the highest-frequency mode again suggests an increase in the Bi-Se distance related to an increase of the Bi coordination from sevenfold in β -Bi₂Se₃ to eightfold in γ -Bi₂Se₃. This result is again in good agreement with the recently observed increase of the Bi coordination on going from β -Bi₂Te₃ to γ -Bi₂Te₃ [41,51].

Figure 10(b) shows the pressure dependence of the experimental and theoretical Raman mode frequencies in γ -Bi₂Se₃. It can be observed that there is a reasonable agreement between the experimental and theoretical Raman mode frequencies and pressure coefficients for this phase. Therefore, we can reasonably suggest that the γ -Bi₂Se₃ phase has the monoclinic C2/c structure already found by means of XRD measurements in Bi₂Te₃ [41] and proposed as a high-pressure phase in Sb₂Te₃ [50]. **Table V** summarizes the experimental and theoretical first-order Raman mode frequencies and pressure coefficients in the γ -Bi₂Se₃ phase at 19.9 GPa.

In our experiments, we have not observed the four lowest frequency modes (A_g^1 , B_g^1 , A_g^2 , and B_g^2), whose detection is difficult because they could be weak in intensity and because their frequencies are below the cutting edge of the Raman edge filter of our spectrometer. Furthermore, they seem to be in a region where we observe several bands that we attribute to interferences from our edge filter [see asterisks in **Fig. 10(a)**]. On the other hand, we have attributed a broad band around 90 cm⁻¹ to the weak modes A_g^3 and B_g^3 . The other seven modes between 150 and 230 cm⁻¹ form a broad band from which we have decomposed six bands [see **Figure 2** in the supplementary material [72)]. We have not evidenced the presence of the B_g^7 mode whose predicted pressure behavior crosses the B_g^6 mode.

As already commented, we have detected a lack of Raman scattering signal above 27.8 GPa thus suggesting a phase transition to a Raman inactive phase above that pressure. The lack of Raman scattering indicates that γ -Bi₂Se₃ undergoes a phase transition towards δ -Bi₂Se₃, and it suggests that the nature of the new phase could be the disordered bcc structure with Im-3m space group recently found in Bi₂Te₃ above 14.4 GPa that dominates the XRD spectrum above 25 GPa [40,41]. The same disappearance of the Raman modes has been recently observed in Sb₂Te₃ and attributed to a transition

to a Raman-inactive phase which could be a disordered bcc (but another phase like a disordered fcc structure cannot be excluded) [50]. Our Raman measurements thus suggest that no phase transition to the monoclinic bcc-like C2/m phase with nine/ten Bi coordination occurs [41]. Note that the main difference between the similar bcc-like C2/m and disordered bcc (Im-3m) structures is that the bcc-like C2/m phase is Raman active, with 12 Raman-active modes, while the Im-3m phase is Raman inactive. Note that on the basis of our Raman measurements we cannot assign δ -Bi₂Se₃ to the disordered bcc structure without ambiguity because it is possible that the Raman scattering signal of the bcc-like C2/m phase is very weak and we have not been able to measure it.

In order to study the structural stability of the different phases of Bi₂Se₃ and to support the previous assignments of the different high-pressure phases of Bi₂Se₃ we have performed total-energy calculations for Bi₂Se₃ with the above proposed structures [40,41]. **Figure 11 (a) and (b)** show the energy vs. volume and the Gibbs free energy difference at 300 K vs. pressure for the different phases calculated. In **Fig. 11(a)** it can be observed that the different phases observed in Bi₂Se₃ under pressure [41] cross each other at reduced volumes and therefore are candidates to be observed at different pressures. Therefore, our assignments of the peak frequencies in the preceding paragraphs to the proposed phases are coherent. The only doubt is whether δ -Bi₂Se₃ is the bcc-like C2/m nine/ten phase or the disordered bcc (Im-3m) phase. Our total-energy calculations support the phase transition from the C2/c phase towards the bcc-like C2/m phase. Unfortunately, we have not been able to make calculations for the disordered bcc phase with Im-3m space group with the VASP code. Therefore, in order to ensure that these phases are consistent we have plotted in **Figure 11(b)** the pressure dependence of the Gibbs free energy difference at T = 300 K for the different monoclinic phases with respect to the R-3m, which is taken as reference. The calculated phase-transition pressure for the R-3m to the C2/m phase is 9 GPa, which compares well with the experimental value (9.7 GPa). The calculated phase-transition pressure for the C2/m to the C2/c phase is around 24.5 GPa while the experimental value obtained from Raman measurements is around 19.9 GPa. Perhaps this disagreement is due to the presence of a slight uniaxial pressure in our Raman experiments leading to a decrease of the phase transition pressure with respect to the value under truly hydrostatic conditions. Finally, as regards the last phase transition, our calculations of enthalpy show that the monoclinic bcc-like C2/m nine-ten structure does not show a smaller enthalpy than the

C2/c phase. This means that in principle a phase transition from the C2/c to the monoclinic bcc-like C2/m phase cannot be observed at T=300K. Furthermore, we have calculated the phonons of the bcc-like C2/m phase at pressures between 25 and 35 GPa and have found that there are phonons with negative frequencies which suggest that this phase is not really stable at those pressures. Therefore, we conclude that it is most likely that the δ -Bi₂Se₃ phase is a disordered bcc phase with Im-3m structure, as already found in Bi₂Te₃ [41] since it is expected that the Gibbs free energy of the disordered bcc structure is even lower than that of the bcc-like C2/m phase. However, the attribution of the δ -Bi₂Se₃ phase to other Raman-inactive phases like a disordered fcc phase cannot be ruled out. Finally, we must comment that it is possible that the phase transition from the C2/c to the Raman inactive phase begins at much lower pressure than 28 GPa, as it is observed by XRD in Bi₂Te₃ [41] since Raman scattering cannot detect it because of the lack of Raman scattering of the latter phase. New XRD measurements at pressures above 20 GPa are needed to establish the onset of the phase transition to the δ -Bi₂Se₃ phase and to determine its crystalline structure.

V. Conclusions

We have performed x-ray diffraction and Raman scattering measurements at room temperature in Bi₂Se₃ up to 20 and 30 GPa, respectively, that have been complemented with *ab initio* total-energy and lattice dynamics calculations. XRD measurements show that the layered-compound α -Bi₂Se₃ undergoes an electronic topological transition in the range 3-5 GPa in which the bulk modulus changes as a consequence of the change of the layer compressibility. Additionally, a phase transition towards a C2/m structure (β phase) is observed between 10 and 12 GPa. On the other hand, Raman scattering measurements indicate that α -Bi₂Se₃ undergoes an ETT near 5 GPa and confirm the transition from the R-3m to the C2/m phase near 10 GPa with an increase in coordination of Bi from 6 to 7. Additionally, two other phase transitions have been observed near 20 and 28 GPa where Bi₂Se₃ is suggested to transform into a C2/c structure (γ phase) and a disordered bcc structure (δ phase), respectively. The four structures here reported for Bi₂Se₃ are the same that have been found previously in Bi₂Te₃ [40,41,51] and Sb₂Te₃ [50]. Our total-energy and lattice dynamics calculations fully support the experimental results here reported and have allowed us to assign the symmetry of most of the Raman-active modes of the high-pressure phases. Finally, we

must note that on fully releasing the pressure the sample returns to the rhombohedral structure below 5 GPa as it occurs also in the related materials Sb_2Te_3 and Bi_2Te_3 [50,51]. We hope the present work will further stimulate new measurements in Bi_2Se_3 under high pressure, especially to fully understand the mechanism of the ETT in the rhombohedral phase and the subtle effects on their structures and properties.

Acknowledgments

This work has been done under financial support from Spanish MICINN under projects MAT2007-66129, MAT2010-21270-C04-03/04, and CSD-2007-00045 and from the Valencian Government (GVA) under project Prometeo/2011-035. It is also supported by the Ministry of Education, Youth and Sports of the Czech Republic (MSM 0021627501). E P-G acknowledges the financial support of the Spanish MEC under a FPI fellowship. Supercomputer time has been provided by the Red Española de Supercomputación (RES) and the MALTA cluster.

References

- [1] G.J. Snyder and E.S. Tober. *Nat. Mater.* **7**, 105 (2008).
- [2] D.M. Rowe, *CRC Handbook of Thermoelectrics* (CRC Press Inc., New York, 1995).
- [3] R. Venkatasubramanian, E. Siivola, T. Colpitts, B. O'Quinn, *Nature* **413**, 597 (2001).
- [4] T.S. Kim, B.S. Chun, J.K. Lee, H. G. Jung, 12th International Symposium on Metastable and Nano-Materials (ISMANAM-2005), Paris, France, July 03-07, 2005; pp 710-713.
- [5] S. Nakajima, *J. Phys. Chem. Solids* **24**, 479 (1963).
- [6] T.J. Scheidemantel, J.F. Meng, and J.V. Badding, *J. Phys. Chem. Solids* **66**, 1744 (2005).
- [7] M. Dresselhaus, G. Dresselhaus, X. Sun, Z. Zhang, S. Cronin, and T. Koga, *Phys. Solid State* **41**, 679 (1999).
- [8] S.S. Hong, W. Kundhikanjana, J.J. Cha, K. Lai, D.S. Kong, S. Meister, M.A. Kelly, Z.X. Shen, and Y Cui, *Nano Lett.* **10**, 3118 (2010).
- [9] D. Teweldebrhan, V. Goyal, M. Rahman, and A. A. Balandin, *Appl. Phys. Lett.* **96**, 053107 (2010).
- [10] D. Teweldebrhan, V. Goyal, and A. A. Balandin, *Nano Lett.* **10**, 1209 (2010).
- [11] H. Steinberg, D.R. Gardner, Y.S. Lee, and P. Jarillo-Herrero, *Nano Lett.* **10**, 5032 (2010).
- [12] K. M. F. Shahil, M. Z. Hossain, D. Teweldebrhan, and A. A. Balandin, *Appl. Phys. Lett.* **96**, 1523103 (2010).
- [13] H. Zhang, C.X. Liu, X.L. Qi, X. Dai, Z. Fang, and S.C. Zhang, *Nature Phys.* **5**, 438 (2009).
- [14] M.Z. Hassan and C.L. Kane, *Rev. Mod. Phys.* **82**, 3045 (2010).
- [15] J.E. Moore, *Nature* **464**, 194 (2010).
- [16] Y. Xia, D. Qian, D. Hsieh, L. Wray, A. Pal, H. Lin, A. Bansil, D. Grauer, Y.S. Hor, R.J. Cava, and M.Z. Hassan, *Nat. Phys.* **5**, 398 (2009).
- [17] H. Zhang, C.X. Liu, X.L. Qi, X. Dai, Z. Fang, and S.C. Zhang, *Nat. Phys.* **5**, 438 (2009).
- [18] Y.L. Chen, J.G. Analytis, J.H. Chu, Z.K. Liu, S.K. Mo, X.L. Qi, H.J. Zhang, D.H. Lu, X. Dai, Z. Fang, S.C. Zhang, I.R. Fisher, Z. Hussain, and Z.X. Shen, *Science* **325**, 178 (2009).

- [19] H. Steinberg, D.R. Gardner, Y.S. Lee, and P. Jarillo-Herrero, *Nano Lett.* **10**, 5032 (2010).
- [20] J. G. Checkelsky, Y.S. Hor, R.J. Cava, and N.P. Ong, *Phys. Rev. Lett.* **106**, 196801 (2011).
- [21] J.V. Badding, J.F. Meng, D.A. Polvani, *Chem. Mater.* **10**, 2889 (1998).
- [22] D.A. Polvani, J.F. Meng, N.V. Chandra Shekar, J. Sharp, and J.V. Badding, *Chem. Mater.* **13**, 2068 (2001).
- [23] N.V. Chandra Shekar, D.A. Polvani, J.F. Meng, and J.V. Badding, *Physica B* **358**, 14 (2005).
- [24] S.V. Ovsyannikov, V.V. Shchennikov, G.V. Vorontsov, A.Y. Manakov, A.Y. Likhacheva, and V.A. Kulbachinskii, *J. Appl. Phys.* **104**, 053713 (2008).
- [25] S.V. Ovsyannikov and V.V. Shchennikov, *Chem. Mater.* **22**, 635 (2010).
- [26] C.-Y. Li, A.L. Ruoff, and C.W. Spencer, *J. Appl. Phys.* **32**, 1733 (1961).
- [27] L.F. Vereshchagin, E.Ya. Atabaeva, and N.A. Bedeliani, *Sov. Phys. Solid State* **13**, 2051 (1972).
- [28] E.Ya. Atabaeva, N.A. Bedeliani, and S.V. Popova, *Fiz. Tverd. Tela* **15**, 3508 (1973); *idem*, *Sov. Phys. Solid State* **15**, 2346 (1974).
- [29] L.G. Khvostantsev, A.I Orlov, N. Kh. Abrikosov, and L.D. Ivanova, *Phys. Stat. Solidi a* **58**, 37 (1980).
- [30] N. Sakai, T. Kajiwara, K. Takemura, S. Minomura, and Y. Fujii, *Solid State Commun.* **40**, 1045 (1981).
- [31] L.G. Khvostantsev, A.I Orlov, N. Kh. Abrikosov, and L.D. Ivanova, *Phys. Stat. Solidi a* **89**, 301 (1985).
- [32] M. Bartkowiak and G.D. Mahan, 18th International Conference on Thermoelectrics, IEEE 713 (1999).
- [33] T. Thonhauser, T.J. Scheidemantel, J.O. Sofo, J.V. Badding, and G.D. Mahan, *Phys. Rev. B* **68**, 085201 (2003).
- [34] T. Thonhauser, *Solid State Commun.* **129**, 249 (2004).
- [35] M. Einaga, Y. Tanabe, A. Nakayama, A. Ohmura, F. Ishikawa, and Yuh Yamada, *J. Phys.: Conf. Ser.* **215**, 012036 (2010).
- [36] J.L. Zhang, S.J. Zhang, H.M. Weng, W. Zhang, L.X. Yang, Q.Q. Liu, S.M. Feng, X.C. Wang, R.C. Yu, L.Z. Cao, L. Wang, W.G. Yang, H.Z. Liu, W.Y. Zhao, S.C. Zhang, X. Dai, Z. fang, and C.Q. Jin, *Proc. Nat. Acad. Sci.* **108**, 24 (2011).

- [37] C. Zhang, L. Sun, Z. Chen, X. Zhou, Q. Wu, W. Yi, J. Guo, X. Dong, and Z. Zhao, *Phys. Rev. B* **83**, 140504 (2011).
- [38] M.K. Jacobsen, R.S. Kumar, A.L. Cornelius, S.V. Sinogeiken, and M.F. Nicol, *AIP Conf. Proc.* **955**, 171 (2007).
- [39] A. Nakayama, M. Einaga, Y. Tanabe, S. Nakano, F. Ishikawa, and Y. Yamada, *High. Press. Res.* **29**, 245 (2009).
- [40] M. Einaga, A. Ohmura, A. Nakayama, F. Ishikawa, Y. Yamada, and S. Nakano, *Phys. Rev. B* **83**, 092102 (2011).
- [41] L. Zhu, H. Wang, Y.C. Wang, J. Lv, Yanmei Ma, Q.L. Cui, Yanming Ma, and G.T. Zou, *Phys. Rev. Lett.* **106**, 145501 (2011).
- [42] E.S. Itskevich, L.M. Kashirskaya, and V.F. Kraidenov, *Semicond.* **31**, 276 (1997).
- [43] A. Polian, M. Gauthier, S.M. Souza, D.M. Trichês, J. Cardoso de Lima, and T.A. Grandi, *Phys. Rev. B* **83**, 113106 (2011).
- [44] I.M. Lifshitz, *Sov. Phys. JETP* **11**, 1130 (1960).
- [45] L. Dagens, *J. Phys. F: Met. Phys.* **8**, 4496 (1978).
- [46] L. Dagens and C. Lopez-Rios, *J. Phys. F: Met. Phys.* **9**, 2195 (1979).
- [47] A.F. Goncharov, V.V. Struzhkin, *Physica B* **385**, 117 (2003).
- [48] D. Antonangeli, D.L. Farber, A.H. Said, L.R. Benedetti, C.M. Aracne, A. Landa, P. Söderlind, and J.E. Klepeis, *Phys. Rev. B* **82**, 132101 (2010).
- [49] D. Santamaria-Perez, A. Vegas, C. Muehle, and M. Jansen, *J. Chem. Phys.* **135**, 054511 (2011).
- [50] O. Gomis, R. Vilaplana, F.J. Manjón, P. Rodríguez-Hernández, E. Pérez-González, A. Muñoz, V. Kucek, and C. Drasar, submitted to *Phys. Rev. B* (2011).
- [51] R. Vilaplana, O. Gomis, F.J. Manjón, A. Segura, E. Pérez-González, P. Rodríguez-Hernández, A. Muñoz, J. González, V. Marín-Borrás, V. Muñoz-Sanjose, C. Drasar, and V. Kucek, *Phys. Rev. B* **84**, 104112 (2011).
- [52] W. Kullmann, J. Geurts, W. Richter, N. Lehner, H. Rauh, U. Steigenberger, G. Eichhorn, and R. Geick, *Phys. Status Solidi B* **125**, 131 (1984).
- [53] H. Köhler and C.R. Becker, *Phys. Stat. Solidi b* **61**, 533 (1974).
- [54] W. Richter, H. Köhler, and C.R. Becker, *Phys. Stat. Solidi b* **84**, 619 (1977).
- [55] H. Rauh, R. Geick, H. Köhler, N. Nücker, and N. Lehner, *J. Phys. C: Solid State Phys.* **14**, 2705 (1981).
- [56] J. Zhang, Z. Peng, A. Soni, Y. Zhao, Y. Xiong, B. Peng, J. Wnag, M.S. Dresselhaus, and Q. Xiong, *Nano Lett.* **11**, 2407 (2011).

- [57] G. Zhang, H. Qin, J. Teng, J. Guo, Q. Guo, X. Dai, Z. Fang, and K. Wu, Appl. Phys. Lett. **95**, 053114 (2009).
- [58] S.Y.F. Zhao, C Beekman, L.J. Sandilands, J.E.J. Bashucky, D. Kwok, N. Lee, A.D. LaForge, S.W. Cheong, and K.S. Burch, Appl. Phys. Lett. **98**, 141911 (2011).
- [59] W. Cheng and S.F. Ren, Phys. Rev. B **83**, 094301 (2011).
- [60] W. Kraus and G. Nolze, J. Appl. Crystallogr. **29**, 301 (1996).
- [61] J. Rodriguez-Carvajal, Physica B **192**, 55 (1993).
- [62] G.J. Piermarini, S. Block, and J.D. Barnett, J. Appl. Phys. **44**, 5377 (1973).
- [63] D. Errandonea, Y. Meng, M. Somayazulu, and D. Hausermann, Physica B **355**, 116 (2005).
- [64] K. Syassen, High Press. Res. **28**, 75 (2008).
- [65] P. Hohenberg and W. Kohn, Phys. Rev. **136**, 3864 (1964).
- [66] G. Kresse and J. Hafner, Phys. Rev. B **47**, 558 (1993); *ibid* **49**, 14251(1994); G. Kresse and J. Furthmüller, Comput. Mat. Sci. **6**, 15 (1996); G. Kresse and J. Furthmüller, Phys. Rev. B **54**, 11169 (1996).
- [67] P. E. Blöchl, Phys. Rev. B **50**, 17953 (Dec 1994). G. Kresse and D. Joubert, Phys. Rev. B **59**, 1758 (1999).
- [68] J. P. Perdew, A. Ruzsinszky, G. I. Csonka, O.A. Vydrov, G.E. Suseria, L.A. Constantin, X Zhou and K. Burke, Phys. Rev. Lett. **100**, 136406 (2008).
- [69] A. Mujica, A. Rubio, A. Muñoz, and R. J. Needs, Rev. Mod. Phys. **79**, 863 (2003).
- [70] M.A. Blanco, E. Francisco, V. Luaña, Comp. Phys. Commun. **158**, 57 (2004).
- [71] K. Parlinski, computer code PHONON. See: <http://wolf.ifj.edu.pl/phonon>.
- [72] See EPAPS Document No. [XXX] for calculation details regarding IR-active modes.
- [73] R. J. Angel, High-Temperature and High-Pressure Crystal Chemistry, Book Series: Reviews in Mineralogy & Geochemistry, vol. **41**, 35 (2000).
- [74] M. Cardona, High Press. Res. **24**, 17 (2004); *idem*, phys. stat. sol (b) **341**, 3128 (2004).
- [75] C. Ulrich, M.A. Mroginiski, A.R. Goñi, A. Cantarero, U. Schwarz, V. Muñoz, and K. Syassen, phys. stat. sol. (b) **198**, 121 (1996).
- [76] A.M. Kubel'kov, H.P. Olijnyk, A.P. Jephcoat, Z.Y. Salaeva, S. Onari, and K.R. Allakverdiev, phys. stat. sol (b) **235**, 517 (2003).

Table I. Calculated (th.) and experimental (exp.) lattice parameters, zero-pressure bulk modulus (B_0), and its derivative (B_0') of Bi_2Se_3 in the R-3m structure at zero pressure and calculated lattice parameters of Bi_2Se_3 in the C2/m and C2/c structures at 13.5 and 25.5 GPa, respectively. Experimental and theoretical values reported in the literature are also provided for comparison.

	a(Å)	b(Å)	c(Å)	β (°)	B_0 (GPa)	B_0'	Refs.
$\alpha\text{-Bi}_2\text{Se}_3$ (0 GPa)							
exp.	4.123(1)		28.486(1)		53(8)	2.9(2)	*
exp.	4.143		28.636				5
th.(GGA-PBESol)	4.127		28.315		47.8	3.9	*
th.(GGA-PBESol) ^a	4.141		28.124		48.0	4.6	*
th.(GGA-PBE)	4.138		28.640				59
th.(GGA-PBE) ^a	4.215		29.828				59
$\beta\text{-Bi}_2\text{Se}_3$ (13.5 GPa)							
exp.	14.007(6)	3.829(1)	8.471(6)	88.31(4)	66(3)	4.5	*
th.(GGA-PBESol)	13.940	3.792	8.420	89.06	60.4	4.8	*
$\gamma\text{-Bi}_2\text{Se}_3$ (25.5 GPa)							
th.(GGA-PBESol)	9.128	6.469	7.191	69.42	77.1	2.6	*

^a Calculations including the SO coupling.

* This work

Table II. Rietveld-refined fractional coordinates corresponding to the high-pressure phase of Bi_2Se_3 at 13.5 GPa. The structure is monoclinic (space group: $C2/m$) with lattice parameters $a = 14.007(6) \text{ \AA}$, $b = 3.829(1) \text{ \AA}$, $c = 8.471(6) \text{ \AA}$ and $\beta = 88.31(4)$.

Atoms	Sites	x	y	z
Bi1	4i	0.023(1)	0	0.194(1)
Bi2	4i	0.234(1)	0	0.221(1)
Se1	4i	0.169(2)	0	0.386(3)
Se2	4i	0.416(2)	0	0.413(4)
Se3	4i	0.359(2)	0	0.000(4)

Table III. Experimental (exp.) room-temperature Raman-mode frequencies and pressure coefficients observed in α -Bi₂Se₃ at both $P_0 = 1$ atm and 5.0 GPa, as obtained from fits to the data using $\omega(P) = \omega(P_0) + a_1 \cdot (P - P_0)$. Theoretical (th.) values calculated at room pressure are also shown for comparison, as well as theoretical and experimental data from Refs. 54, 56, and 59, respectively.

Mode	$\omega(P=P_0)$	a_1	$\omega(P=P_0)$	a_1	$\omega(P=P_0)$	$\omega(P=P_0)$	$\omega(P=P_0)$
	(exp.) (cm ⁻¹)	(exp.) (cm ⁻¹ /GPa)	(th.) (cm ⁻¹)	(th.) (cm ⁻¹ /GPa)	(exp.) (cm ⁻¹)	(th.) (cm ⁻¹)	(th.) (cm ⁻¹)
E _g ¹			41.8	1.47	37	42.1	38.9
A _{1g} ¹	72.2(5) ^a	3.2(1) ^a	74.4	2.53	72	74.6	63.85
	88.3(3) ^b	1.98(1) ^b					
E _g ²	131.4(6) ^a	4.1(1) ^a	136.2	3.13	131	138.9	124.0
	153.5(3) ^b	2.3(3) ^b					
A _{1g} ²	174(1) ^a	2.92(2) ^a	174.3	2.68	174	179.5	166.4
	188.3(7) ^b	2.65(7) ^b					
Refs.	*	*	*	*	54,56	59 ^c	59 ^d

* This work.

^a Calculated at room pressure ($P_0 = 1$ atm)

^b Calculated at $P_0 = 5.0$ GPa.

^c GGA calculations without SO coupling.

^d GGA calculations with SO coupling.

Table IV. Experimental (exp.) Raman-mode frequencies and pressure coefficients observed in β -Bi₂Se₃ at room temperature at $P_0= 9.8$ GPa as obtained from fits using $\omega(P) = \omega(P_0) + a_1 \cdot (P-P_0)$. Theoretical (th.) *ab initio* values for the frequencies and pressure coefficients at 9.8 GPa are also shown for comparison.

Mode	$\omega(P_0)$ (exp.) (cm ⁻¹)	a_1 (exp.) (cm ⁻¹ /GPa)	$\omega(P_0)$ (th.) (cm ⁻¹)	a_1 (th.) (cm ⁻¹ /GPa)
B _g ¹			35.5	0.48
A _g ¹			45.0	0.99
B _g ²			50.1	0.61
A _g ²			55.4	0.52
A _g ³	78(2)	0.68(7)	82.7	0.39
A _g ⁴	98(2)	2.76(5)	104.1	1.79
B _g ³	138(3)	1.69(4)	134.0	1.47
B _g ⁴	143(2)	1.3(1)	144.7	0.42
A _g ⁵	141(2)	3.0(1)	142.1	1.85
A _g ⁶	157(1)	2.07(9)	151.6	2.01
A _g ⁷	160(3)	2.1(2)	157.1	2.08
B _g ⁵			161.7	1.16
A _g ⁸	172(2)	2.12(9)	176.4	1.85
A _g ⁹	192(2)	1.95(6)	190.7	1.67
A _g ¹⁰	198(3)	2.11(7)	198.7	2.18

Table V. Experimental (exp.) Raman-mode frequencies and pressure coefficients observed in γ -Bi₂Se₃ at room temperature at $P_0=19.9$ GPa as obtained from fits using $\omega(P) = \omega(P_0) + a_1 \cdot (P-P_0)$. Theoretical (th.) *ab initio* values for the frequencies and pressure coefficients at 19.9 GPa are also shown for comparison.

Mode	$\omega(P_0)$ (exp.) (cm ⁻¹)	a_1 (exp.) (cm ⁻¹ /GPa)	$\omega(P_0)$ (th.) (cm ⁻¹)	a_1 (th.) (cm ⁻¹ /GPa)
B _g ¹			35.8	0.27
A _g ¹			47.0	0.63
B _g ²			57.8	-0.24
A _g ²			68.3	0.74
B _g ³	91(5)	0.8(2)	80.2	1.18
A _g ³	91(5)	0.8(2)	82.6	0.61
B _g ⁴	114(4)	2.1(1)	126.4	2.26
A _g ⁴	122(4)	2.7(3)	134.8	2.36
B _g ⁵	156(4)	2.6(2)	152.9	2.38
B _g ⁶	172(4)	3.0(2)	164.3	2.90
A _g ⁵	182(4)	2.8(4)	175.2	2.76
B _g ⁷			174.8	1.20
A _g ⁶	196(3)	2.0(2)	192.3	2.02
B _g ⁸	201(4)	2.0(2)	200.7	1.93
A _g ⁷	210(4)	1.8(1)	203.3	1.92

Figure captions

Fig. 1. Selected X-ray powder diffraction patterns of Bi_2Se_3 at different pressures showing the low and high pressure phases of Bi_2Se_3 . Backgrounds have been subtracted. Arrows indicate the appearance of new diffraction peaks corresponding to the high pressure phase ($\beta\text{-Bi}_2\text{Se}_3$). The spectrum at room pressure (RP) after releasing pressure from 20 GPa is also shown.

Fig. 2. (color online) Observed (solid circles), calculated and difference (solid lines) XRD profiles of the high-pressure phase of Bi_2Se_3 at 13.5 GPa. Vertical markers indicate Bragg reflections. The R_{Bragg} , R_{wp} and R_{p} residuals are 3.36%, 16.4% and 12.5%, respectively. Lattice parameters and atomic positions are collected in **Table II**.

Fig. 3. (color online) Pressure dependence of the unit-cell volume for both the low-pressure ($R\text{-}3m$) and the high-pressure ($C2/m$) phases of Bi_2Se_3 under compression. Experimental volume per unit formula for the low- and high-pressure phases as a function of pressure are represented by solid black squares and blue circles, respectively. Dashed and solid lines show the fit to a Birch-Murnaghan equation of state for experimental and theoretical data, respectively. Error bars for experimental data are smaller than experimental data points.

Fig. 4. (color online) (a) Pressure dependence of the lattice parameters for the low-pressure ($R\text{-}3m$). Inset shows the c/a ratio vs. pressure dependence. (b) Pressure dependence of the lattice parameters for the high-pressure ($C2/m$) phases of Bi_2Se_3 . Experimental and theoretical data are represented by symbols and lines, respectively. Error bars for experimental data are smaller than experimental data points.

Fig. 5. Dependence of the reduced pressure H vs. the Eulerian strain f_{E} (a). Idem for H_{a} (b) and H_{c} (c). Straight lines represent linear fits to the data points in two different regions for (a) and (b) and in the whole region for (c) panels.

Fig. 6. Experimental Raman spectra of $\alpha\text{-Bi}_2\text{Se}_3$ at pressures between 1 atm and 8.6 GPa.

Fig 7. (color online) (a) Experimental pressure dependence of the Raman mode frequencies in α -Bi₂Se₃. Solid (dashed-dotted) curves represent *ab initio* calculated mode frequencies of modes observed (not observed) in our measurements. Dashed lines represent a different behaviour of the experimental Raman mode with pressure. Error bars for experimental data are smaller or equal than experimental data points. (b) Experimental pressure dependence of the full width half medium (FWHM) of the Raman modes. Solid lines represent two different behaviours of the FWHM with pressure.

Fig. 8. (Color online) Experimental (red squares) and theoretical (black circles) frequencies of the Raman-active modes of α -Bi₂Se₃, α -Bi₂Te₃, and α -Sb₂Te₃ as a function of the total mass (a) and the reduced mass (b) of the AX (A=Sb,Bi; X=Se,Te) molecule. Error bars for experimental data are smaller or equal than experimental data points.

Fig. 9. (Color online) (a) Experimental Raman spectra of the high-pressure phase of β -Bi₂Se₃ at pressures between 9.8 and 18.7 GPa. Bottom marks indicate the calculated frequencies of the Raman-active modes in the β -Bi₂Se₃ phase at 9.8 GPa. Asterisks mark the Raman peaks remaining from the R-3m phase at 9.8 GPa. (b) Experimental pressure dependence of the Raman mode frequencies in β -Bi₂Se₃. Solid (dashed-dotted) curves represent *ab initio* calculated mode frequencies of modes observed (not observed) in our measurements.

Fig. 10. (Color online) (a) Experimental Raman spectrum of γ -Bi₂Se₃ at pressures between 19.9 and 27.8 GPa and at ambient pressure after releasing pressure. Bottom marks indicate the calculated frequencies of the Raman-active modes in the γ -Bi₂Se₃ phase at 19.9 GPa. (b) Experimental pressure dependence of the Raman mode frequencies in γ -Bi₂Se₃. Solid (dashed-dotted) curves represent *ab initio* calculated mode frequencies of modes observed (not observed) in our measurements. Asterisks are likely interferences from our edge filter (see text).

Fig. 11. Theoretical calculation of energy vs. volume (a) and Gibbs free energy difference vs. pressure at 300 K (b) for the R-3m, C2/m, C2/c, and bcc-like C2/m phases of Bi_2Se_3 . Free energy of R-3m phase is taken as reference in (b).

Fig. 1

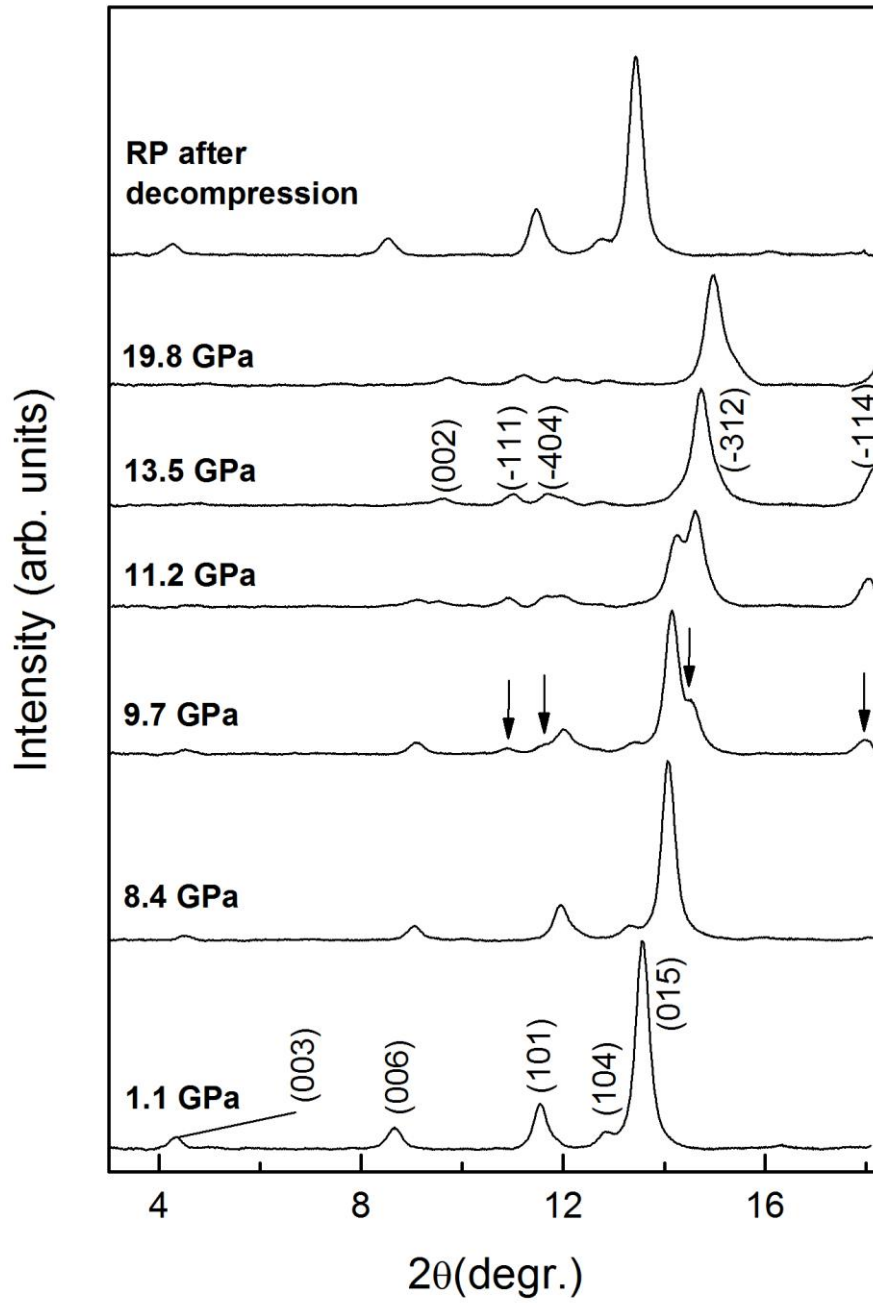


Fig. 2.

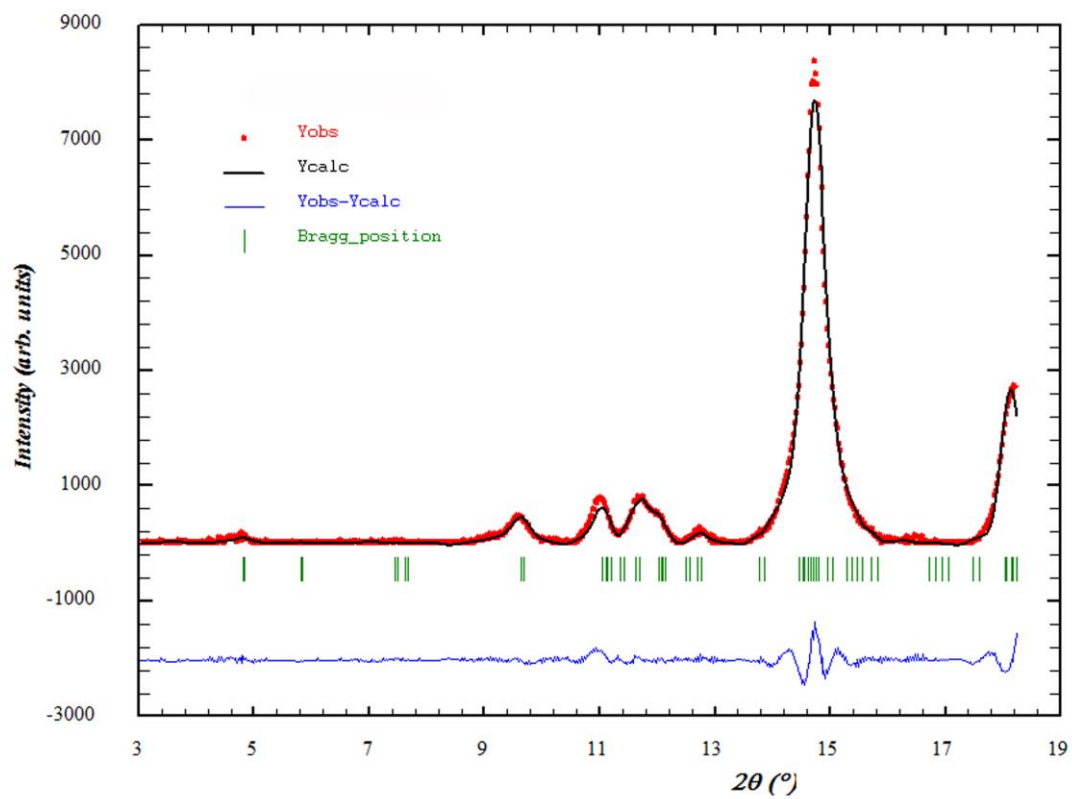


Fig. 3.

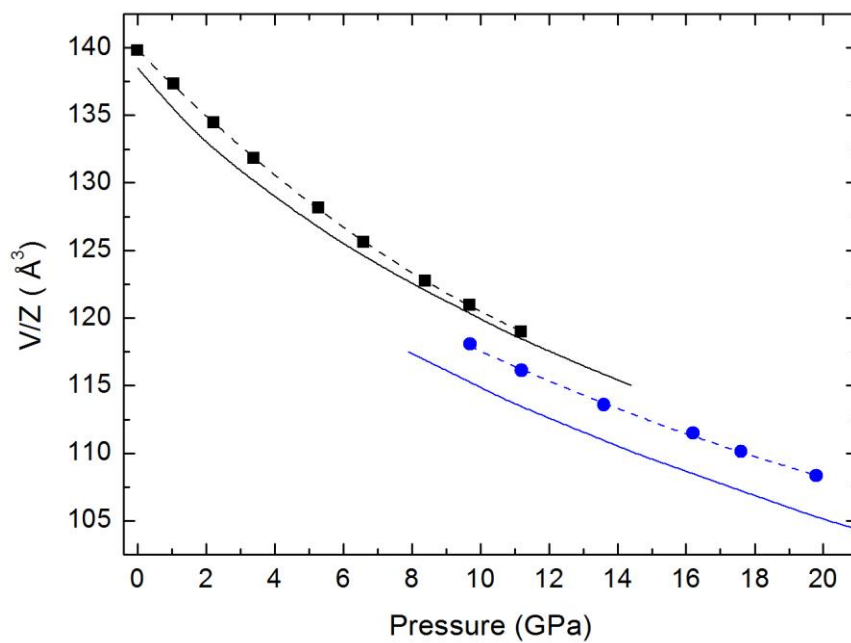


Fig. 4(a)

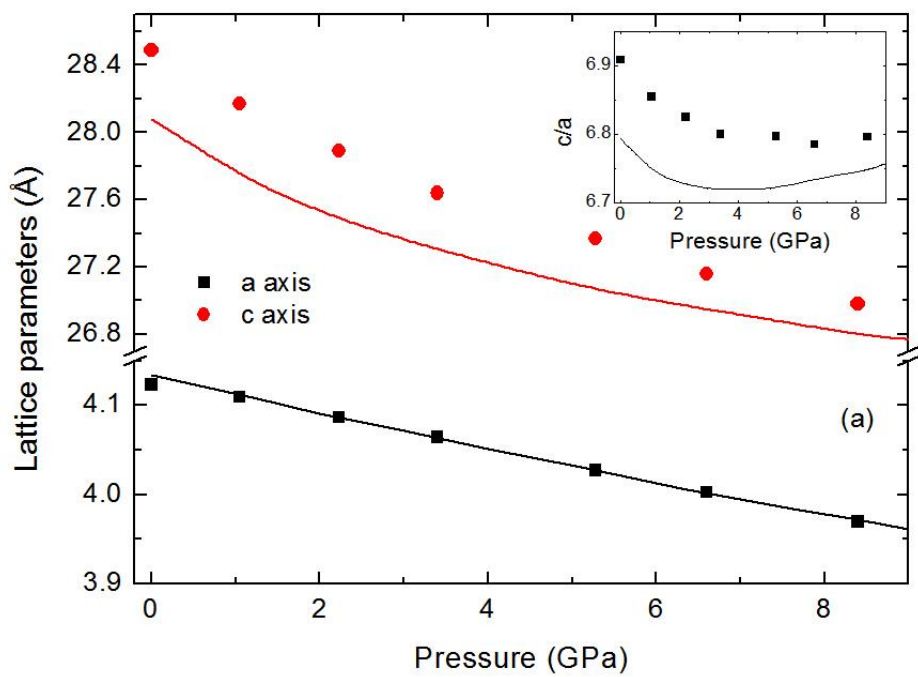


Fig. 4(b)

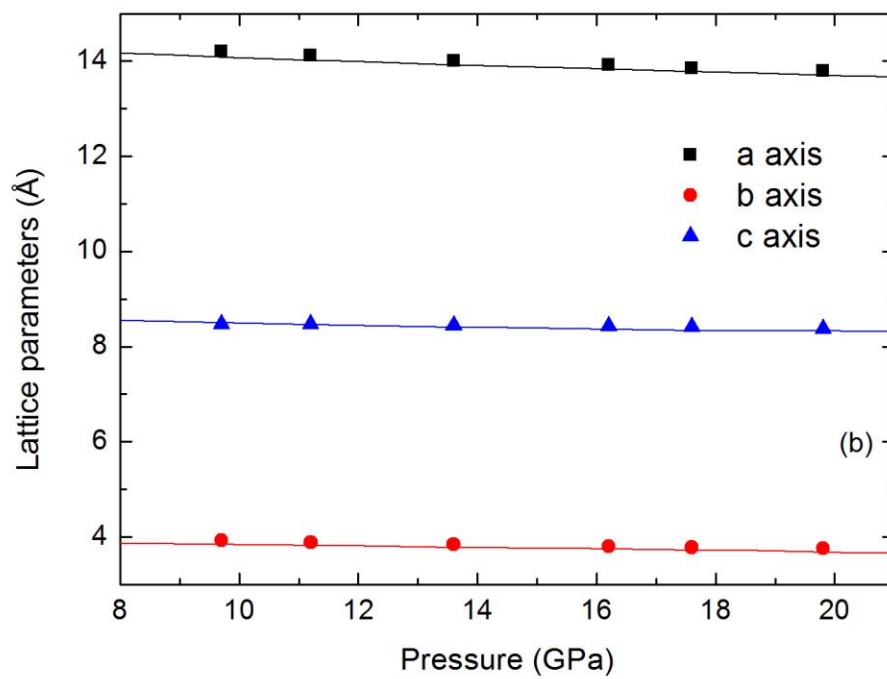


Fig. 5.

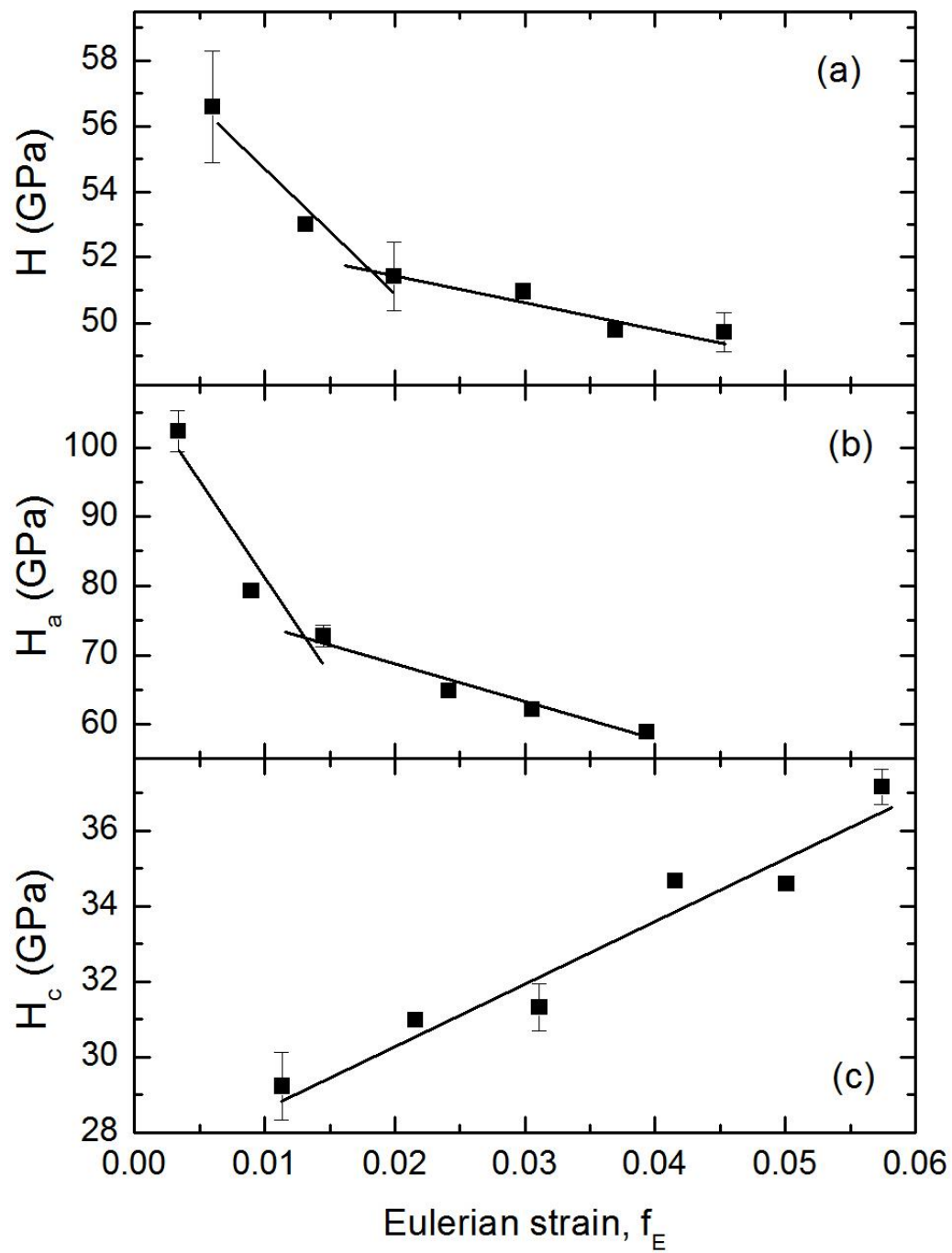


Fig. 6

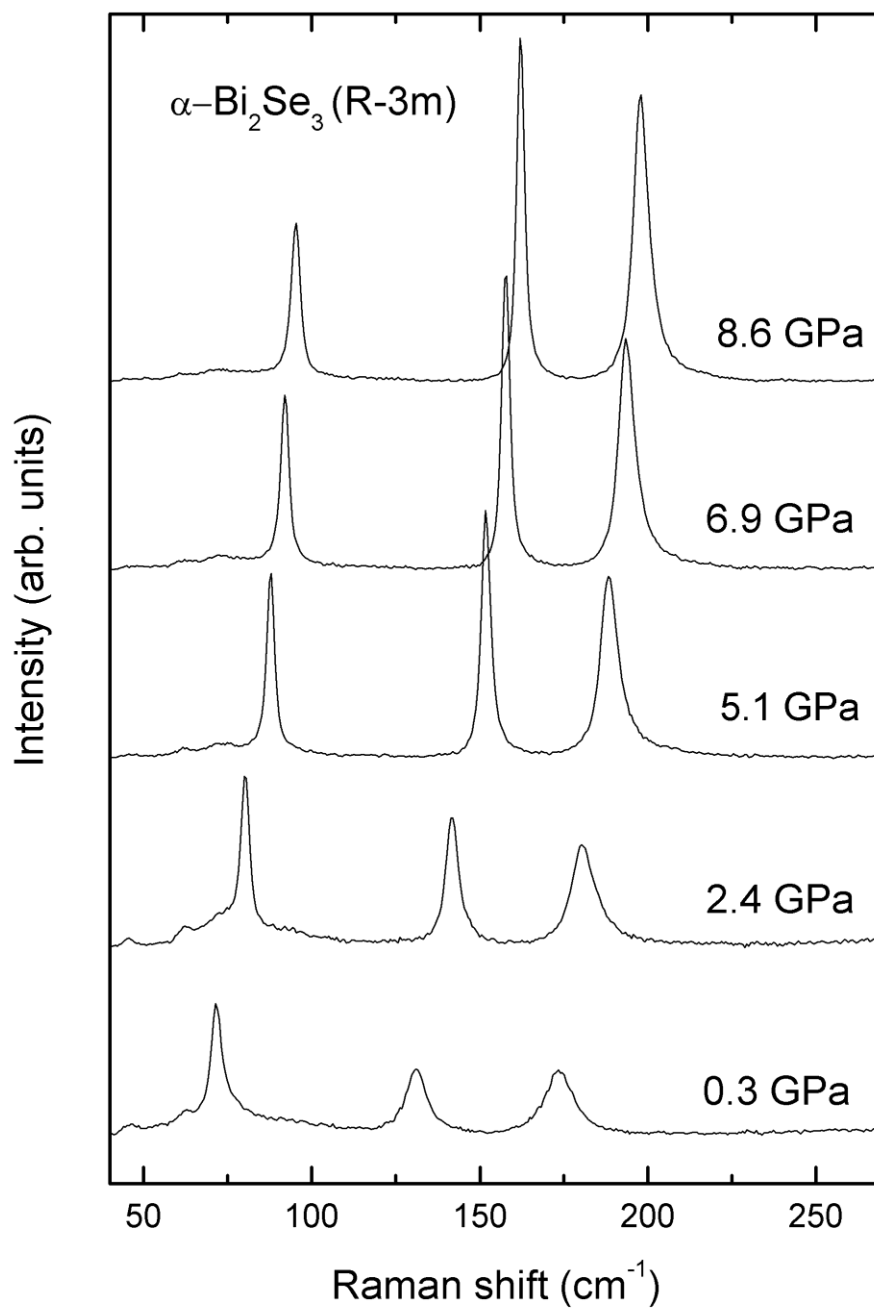


Fig. 7(a)

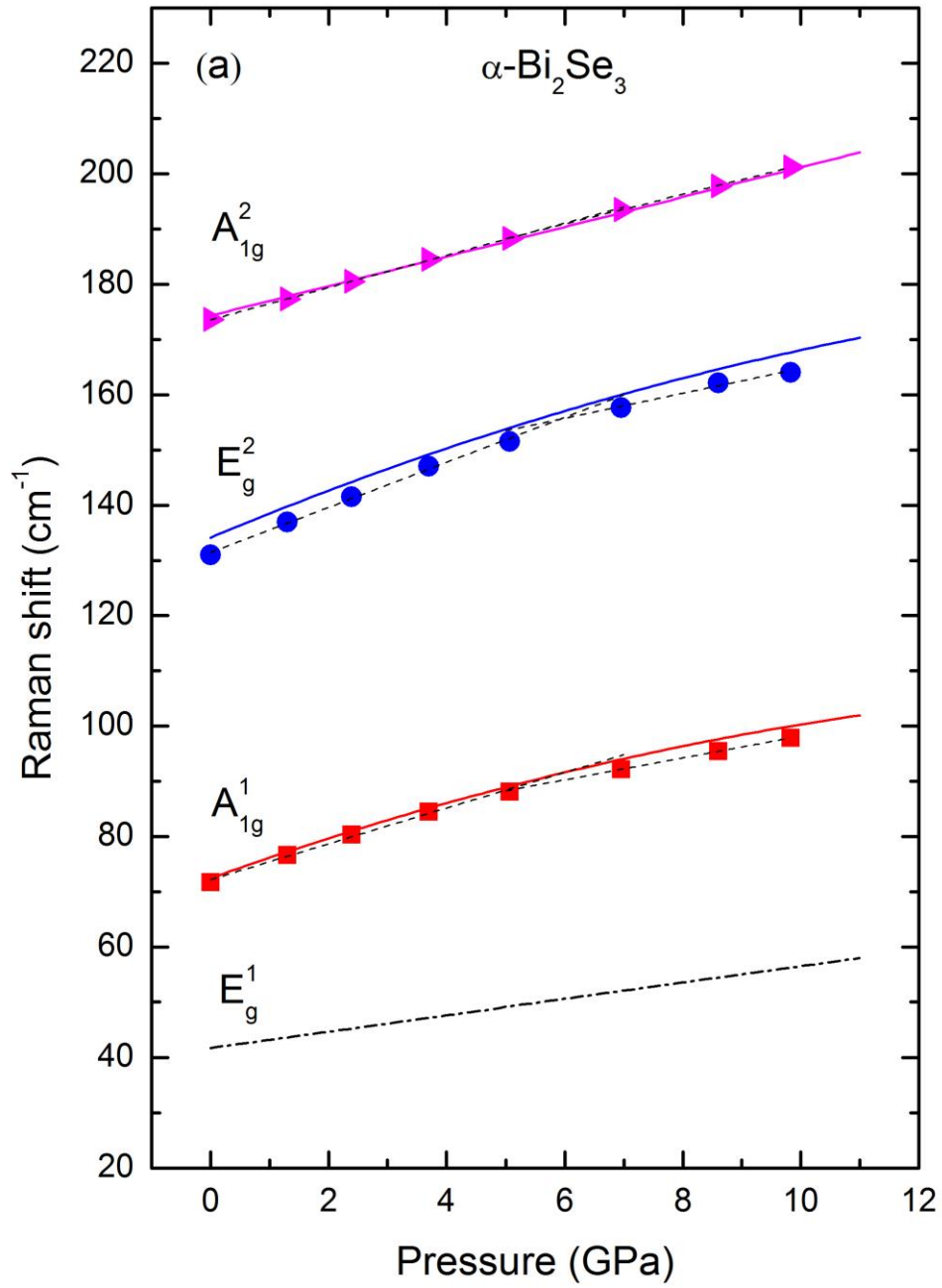


Fig. 7(b)

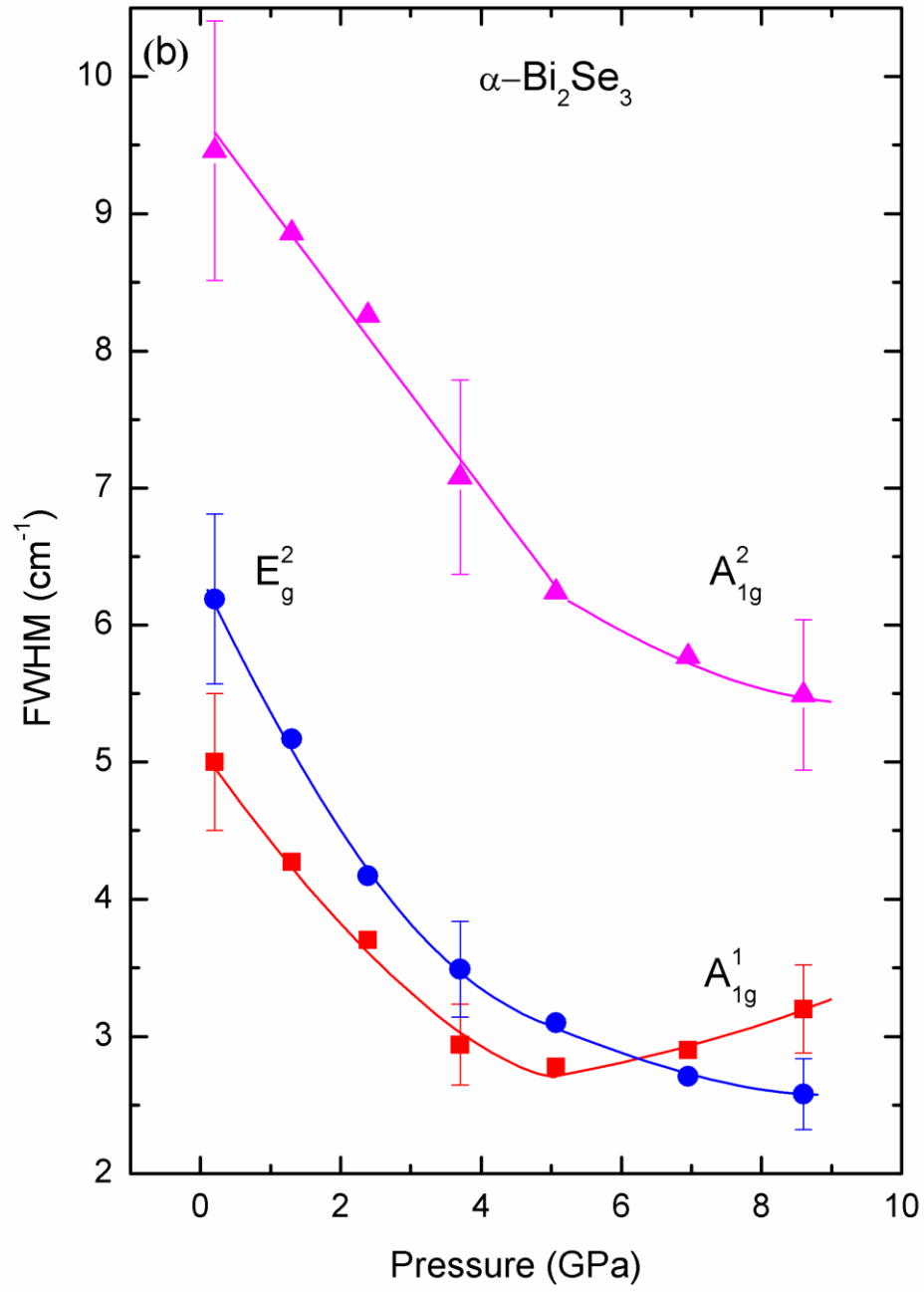


Fig. 8

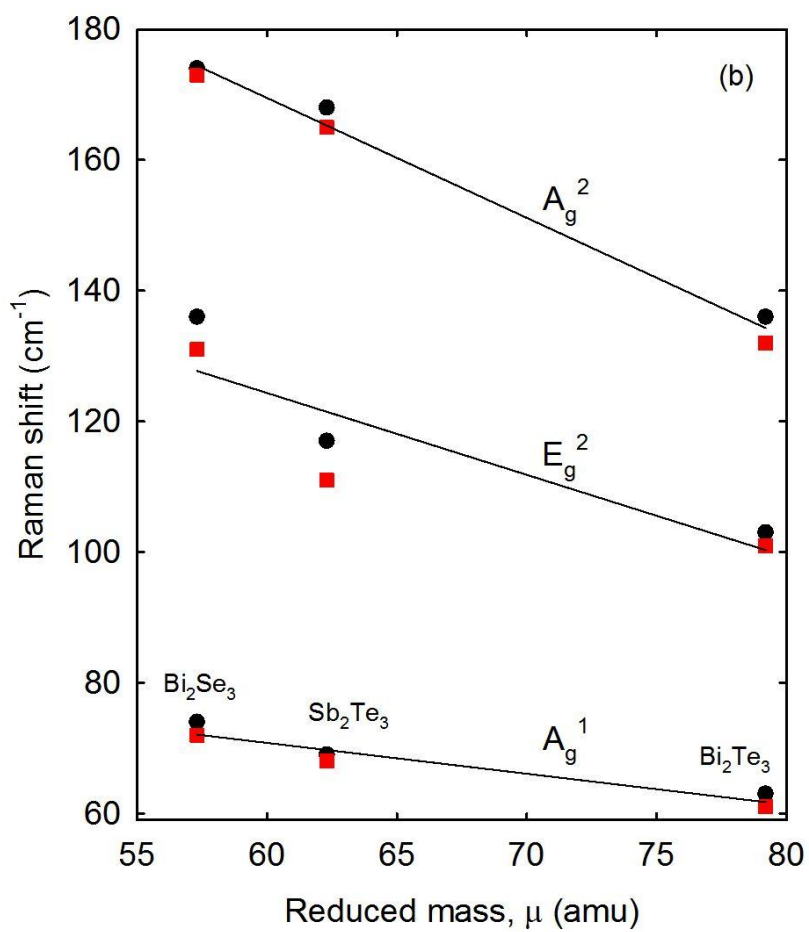
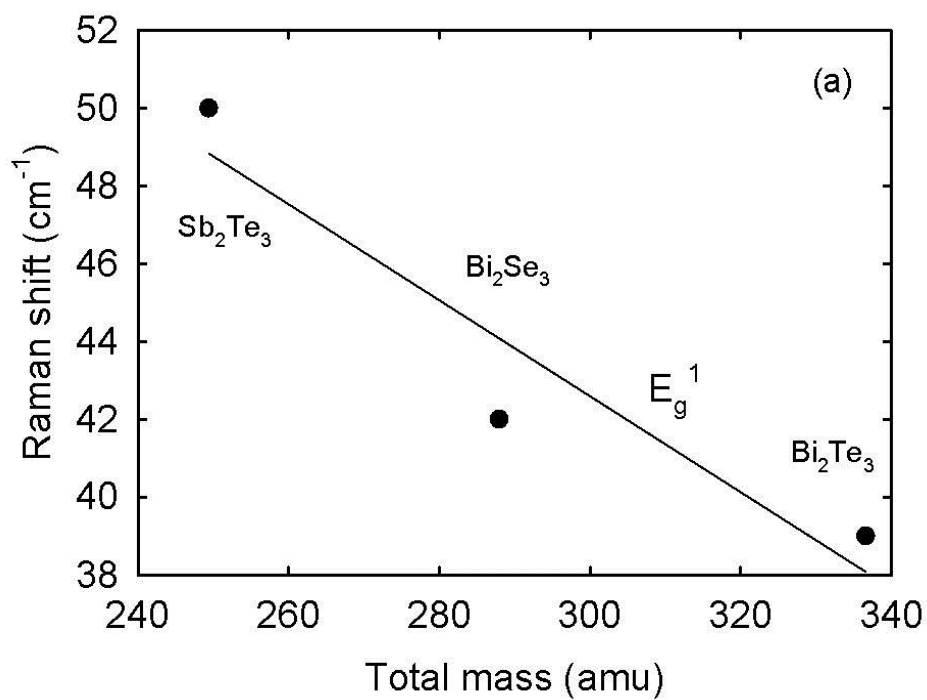


Fig. 9(a)

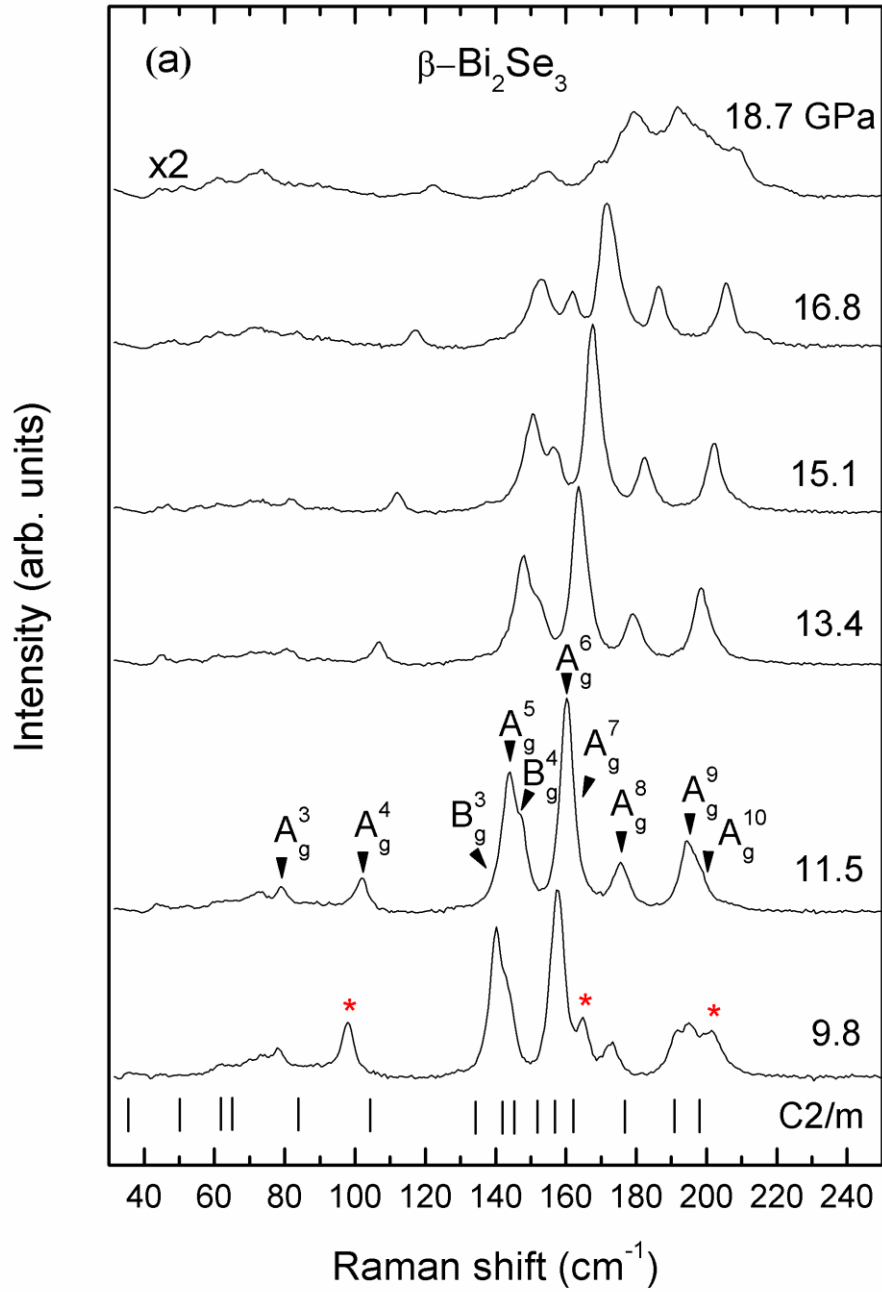


Fig. 9(b)

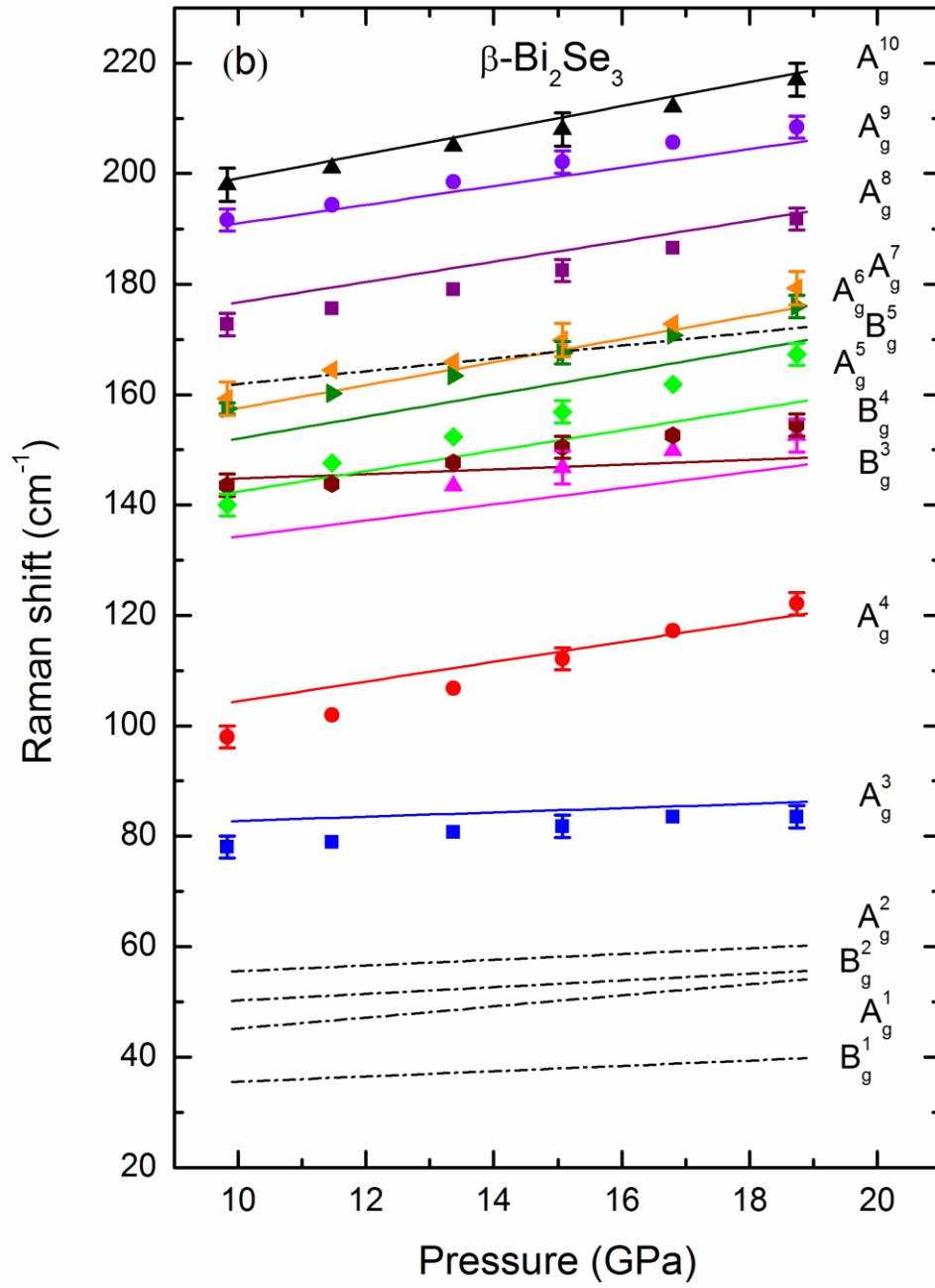


Fig. 10(a)

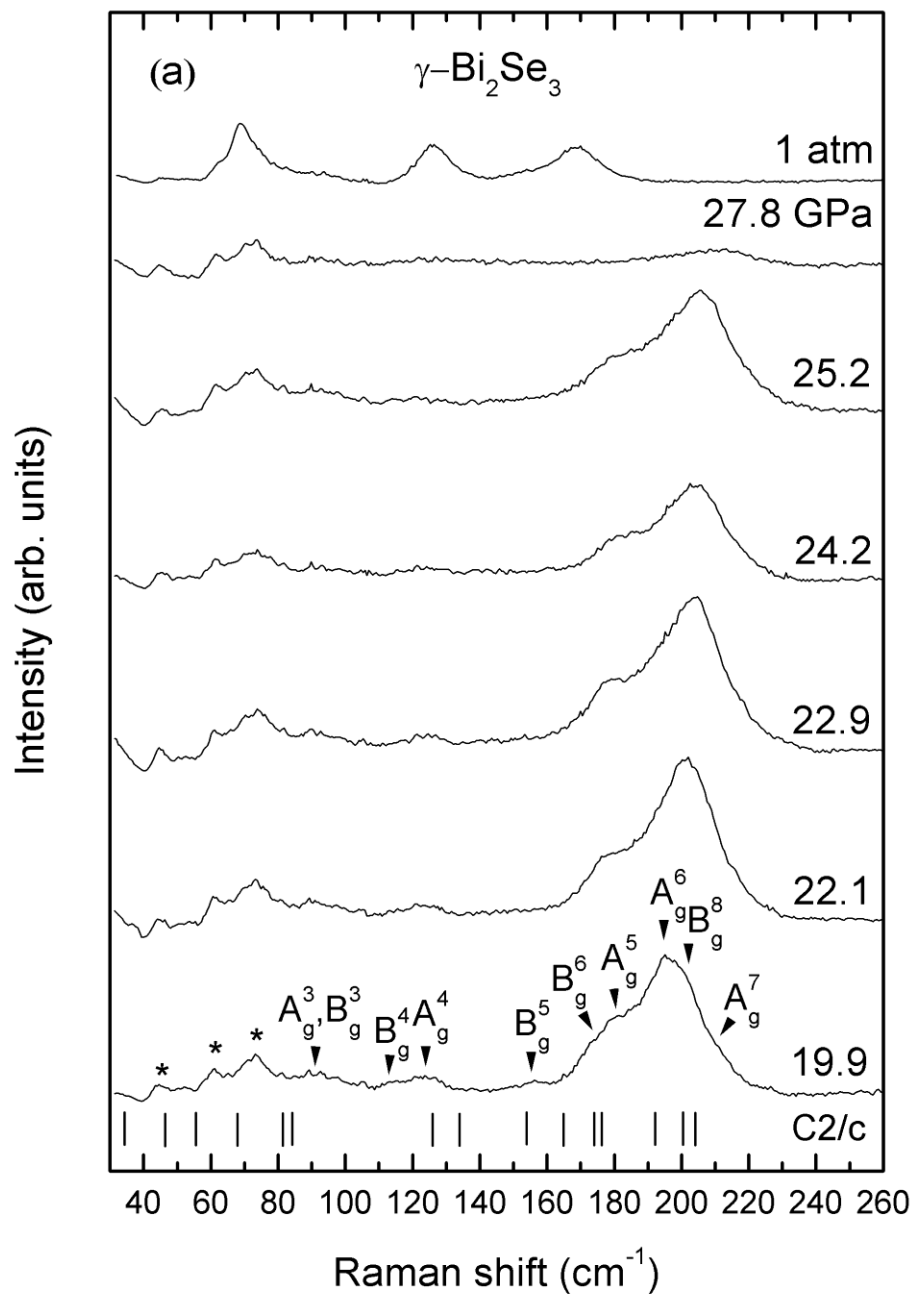


Fig. 10(b)

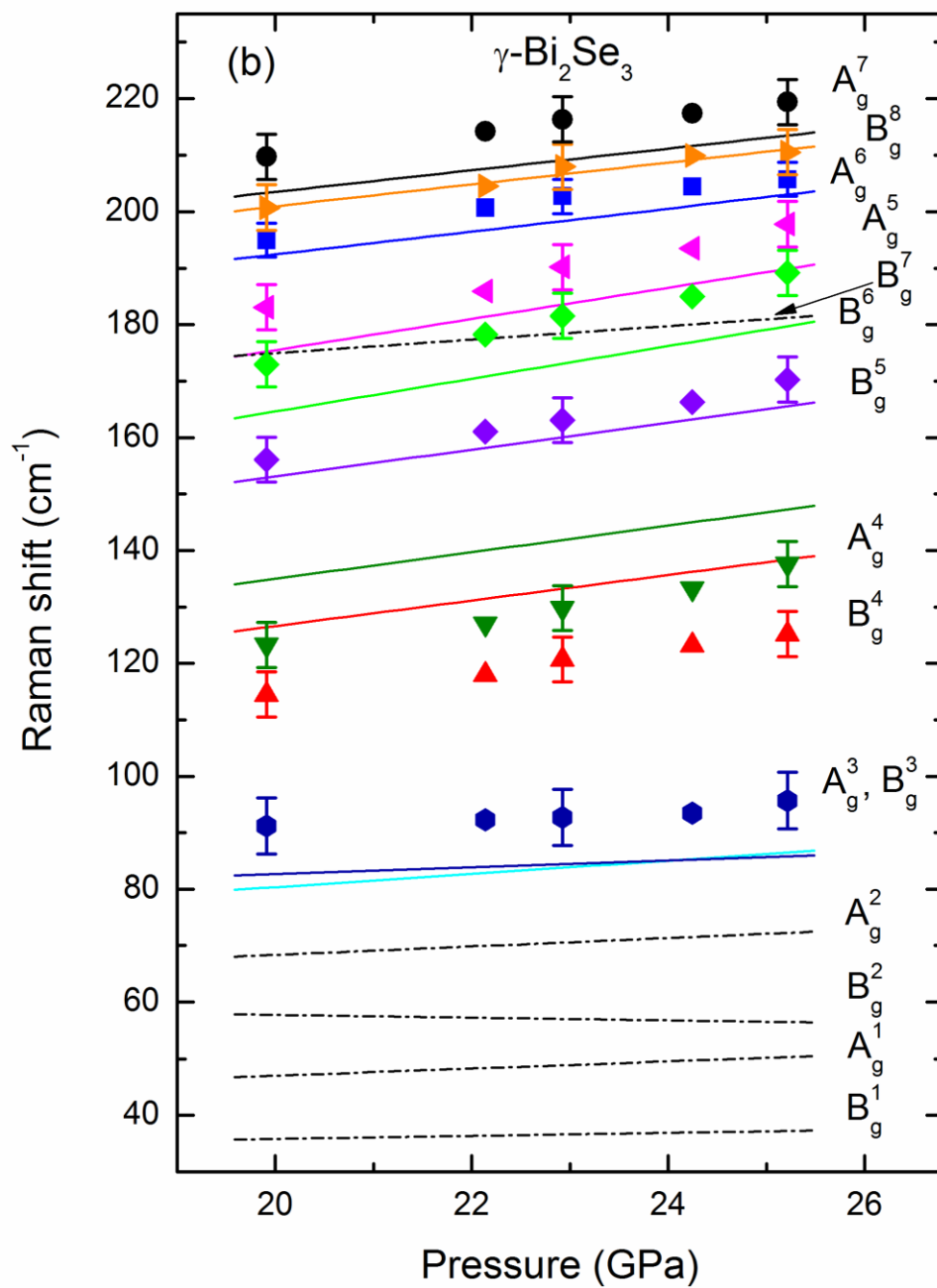


Fig. 11(a)

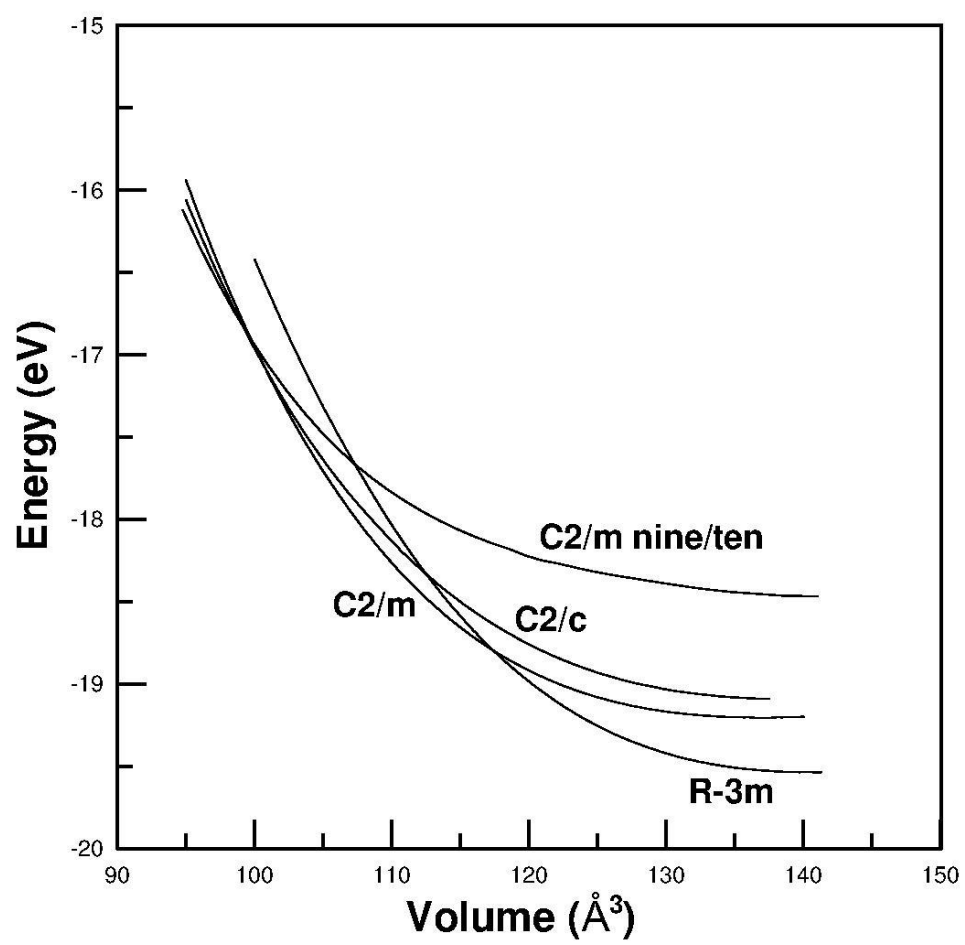


Fig. 11(b)

